Scanning Standing-Wave Illumination Microscopy: A Path to Nanometer Resolution in X-ray Microscopy

by

Stanley S. Hong

S.B., Electrical Engineering and Computer Science
Massachusetts Institute of Technology, 2000

M.Eng., Electrical Engineering and Computer Science
Massachusetts Institute of Technology, 2001

Submitted to the Department of
Electrical Engineering and Computer Science
in partial fulfillment of the requirements for the degree of

Doctor of Philosophy

at the

Massachusetts Institute of Technology

February 2005

Author .....
Department of Electrical Engineering and Computer Science
November 22, 2004

Certified by .....
Dennis M. Freeman
Associate Professor
Thesis Supervisor

Accepted by .....
Arthur C. Smith
Chairman, Department Committee on Graduate Students

Scanning Standing-Wave Illumination Microscopy: A Path to Nanometer Resolution in X-ray Microscopy

by

Stanley S. Hong

Submitted to the Department of Electrical Engineering and Computer Science
on November 22, 2004 in partial fulfillment of the
requirements for the degree of
Doctor of Philosophy

Abstract

X-ray microscopy can potentially combine the advantages of light microscopy with resolution approaching that of electron microscopy. In theory, x-ray microscopes can image unsectioned hydrated cells with nanometer resolution. In practice, however, the resolution of x-ray microscopes is limited to approximately 20 nm due to difficulties in the construction of high numerical-aperture (NA) x-ray focusing optics. This thesis represents a step on a new path to nanometer resolution in x-ray microscopy by proposing and demonstrating scanning standing-wave illumination (SWI) microscopy. In scanning SWI microscopy, lensless focusing is achieved with the interference of large numbers of phase-aligned planar wavefronts. Resolution is determined primarily by the NA synthesized by the planar wavefronts, circumventing the need for high-NA optical components.

Both theoretical and experimental work conducted at visible wavelengths is presented. An electromagnetic theory of image formation in scanning SWI fluorescence microscopy is developed. The point spread function is remarkably well-suited to Fourier analysis and can be analyzed using graphical techniques. Phase alignment is accomplished by maximizing the intensity of light scattered or fluoresced by a point-like particle using an iterative algorithm that is guaranteed to converge monotonically. A prototype scanning SWI microscope with 15 phase-modulated linearly-polarized laser beams arranged in a 0.95-NA radially-polarized circular cone and a 0.25-NA objective lens is presented. Sub-wavelength resolution according to both classical resolution criteria (i.e., measurement of the point-spread function) and modern resolution criteria (i.e., investigation of limits imposed by noise in computationally restored images) is demonstrated.

Thesis Supervisor: Dennis M. Freeman
Title: Associate Professor

Acknowledgments

First and foremost, I would like to thank Professor Dennis Freeman. Since I started working in his lab as a sophomore, he has taught me virtually everything I know about doing research and, perhaps more importantly, about writing, presenting, teaching, and mentoring. He was both the person pushing me onto the tightrope and the safety net. He has the courage and wisdom to explore new ideas and to give students the freedom to work them out. I look forward to seeing where the next new idea takes us.

This thesis would never have been finished without Professors Henry Smith and Peter So. I thank them for their enthusiasm, honesty, and patience. Writing this thesis for them was truly a pleasure, and our committee meetings were the highlights of my thesis experience.

I would like to thank Michael Mermelstein for inventing synthetic aperture microscopy and for welcoming me into his optics lab at just the right time. He showed me that there is a wrong way, a right way, and a super-cool way of doing things in the lab.

I would like to thank Professor Berthold Horn, whose theoretical insights permeate this thesis. I thank him for his enthusiasm, creativity, and for allowing me to benefit from his astounding clarity of thought.

I would also like to thank Cameron Abnet and Joseph Deck for their help and advice in building the new microscope, John Fini and Jekwan Ryu for their work on synthetic aperture microscopy, and A. J. Aranyosi for his smooth optimism and for keeping our Linux network in tip-top condition. I would also like to thank my fellow eighth floor residents Salil Desai, Amy Englehart, Kinu Masaki, Rooz Ghaffari, Bennett Landman, Wendy Gu, Aleem Siddiqui, Chris Bergevin, and Janice Balzer for their help and support, especially during the week before my defense.

Finally, I would like to thank my fiancé Annie Chan for her patience, understanding, and support, and Mom, Dad, Alice, and Alvin for always believing in me.

Contents

List of Figures

Chapter 1

Introduction

1.1 A case for photons

Less poetically, the coincidence in energy of visible photons and of the majority of valence electron transitions makes the optical regime of the electromagnetic spectrum unique.

(Pohl and Novotny, 1994 [1])

If resolution was all that mattered, by now all optical microscopes would have been completely supplanted by more modern microscopes. The resolutions of electron and scanning probe microscopes have reached atomic scales, while the resolution of the venerable optical microscope has been largely limited to hundreds of nanometers for a century. However, the optical microscope continues to be an indispensable scientific instrument, especially in the investigations of the life sciences.

A principal reason for the longevity of the optical microscope is its ability to study live specimens. Higher resolution microscopy techniques often require preparation methods that kill specimens and destroy delicate structures; they can only provide snapshots of what survives preparation. To borrow an analogy from Lichtman and Fraser [2], biological investigation is often analogous to attempting to figure out the rules of a complex game like American football. Studying thousands of photographs taken from thousands of different games would provide a wealth of detail. However,

invaluable insight would still be gained by watching a single game in its entirety on television (albeit at lower resolution).

One could also argue that light is simply "unique." Biological materials intrinsically interact with light and provide natural contrast mechanisms. Most materials readily reflect and absorb light, providing the option of epi- or transmitted-light imaging. Materials also possess significant variations in refractive index, enabling phase contrast, differential interference contrast, and polarization microscopy. Contrast is often strongly dependent on wavelength, which produces color and enables spectroscopic analysis. Also, recent advances in fluorescence techniques have vastly improved upon traditional contrast enhancement techniques (such as staining) and have become a topic of intense research activity [3].

The uniqueness of light has also enabled revolutionary light sources and light detectors. The invention of the laser made coherent light practical and led to a wide range of scientific achievements, such as temporal resolutions of several femtoseconds and the realization of Bose-Einstein condensates [4, 5, 6]. Photoelectric effect also makes electronic detection of light possible, enabling applications such as fiber-optic communication and digital image processing.

In the past decade, a new technique in optical microscopy was developed that stands at the intersection of fluorescence, coherent light, electronic imaging, and computation. In 1993, Bailey and Lanni demonstrated that the axial resolution of a fluorescence microscope could be improved with structured illumination generated by the interference of two laser beams [7]. Since then, the physical principle has been put on solid theoretical footing and has been demonstrated experimentally in numerous configurations [8, 9, 10, 11, 12, 13, 14, 15, 16, 17, 18, 19].

Previously reported work in standing-wave illumination (SWI) microscopy has focused on using the pairwise interference of two to four planar wavefronts. However, there are unique advantages to using larger numbers of wavefronts which remain largely unexplored. In particular, resolution in an optical microscope is determined by the numerical aperture (NA) of the imaging optics *and* of the illumination optics; in theory, a SWI microscope with a large number of wavefronts could derive its resolution

almost entirely from its illumination. This theoretical curiosity could potentially solve a long-standing problem in microscopy.

1.2 The dream

At one point, x-ray microscopy was considered the successor to optical microscopy [20, 21, 22, 23]. Because resolution is proportional to wavelength (all other things being equal), the development of x-ray microscopy appeared to be a straightforward way to increase resolution while retaining all the benefits of optical microscopy. The discovery of the "water window" at soft x-ray wavelengths (2.3–4.4 nm, where water is an order of magnitude more transparent than biological material) generated much interest, offering the potential for imaging live specimens with molecular resolution. However, scientists soon realized that x-rays are not readily refracted or reflected by any optical material. Also, the short wavelength of x-rays was a double-edged sword; because high-NA imaging optics require curved surfaces accurate to a fraction of a wavelength, construction of a high-resolution soft x-ray microscope demanded fabrication tolerances of less than a nanometer. A high-resolution soft x-ray microscope could not be built.

For decades, the resolutions of soft x-ray microscopes did not exceed those of visible-light microscopes [24, 25]. Recent advances in microfabrication and the advent of coherent x-ray sources have enabled the development Fresnel zone-plate x-ray objectives with reported resolutions of 20 nm [26, 27]. However, further improvement of zone-plate resolution may not be possible [28]. Several novel methods for improving resolution have been proposed including the use of higher diffracted orders in zone plates [28], x-ray diffraction microscopy [29], and photon sieves [30]. However, the results of these efforts remain uncertain.

In spite of past difficulties, an x-ray microscope with nanometer resolution is needed now perhaps more than ever. The structure and function of deoxyribonucleic acid (DNA) has been the rage of mainstream science in past decades. The DNA frenzy culminated in a race to sequence the human genome. We now know that the

one-dimensional base-pair sequence alone is not enough to fully understand the role of DNA; the *three*-dimensional shapes of the proteins which the DNA encodes are thought to be the key to understanding the molecular basis of life [31, 32]. While numerous celebrated techniques exist for deducing the shapes of proteins such as x-ray crystallography (Nobel Prize 1915, 1958, 1962, 1964, and 1985) and nuclear magnetic resonance (Nobel Prize 1952, 1991, and 2002), they cannot study proteins in their natural states and furthermore are not *imaging* techniques. In theory, a soft x-ray microscope could image hydrated intact cells with molecular resolution. However, the construction of such a microscope has been an elusory dream.

1.3 A new path

This thesis represents a step on a new path to constructing an x-ray microscope with nanometer resolution. The objective of the thesis is to demonstrate that sub-wavelength resolution can be achieved with only low-NA optics by using SWI generated by large numbers of planar wavefronts. The thesis extends existing work in SWI microscopy by developing the theoretical and experimental techniques required to prove the concept at visible wavelengths with fluorescence imaging and by recognizing the potential for scaling the technique to x-ray wavelengths.

This thesis is written as a sequence of four journal manuscripts. While each chapter is sufficiently independent to stand alone, as a whole they summarize effort toward the singular objective. Chapter 2 establishes the theoretical foundation of the thesis by developing a theory of image formation in scanning SWI fluorescence microscopy. Chapter 3 describes the construction and testing of an apparatus for generating and controlling SWI which can be scaled to x-ray wavelengths. Chapter 4 solves the critical problem of phase alignment, a new problem in SWI microscopy created by the use of large numbers of wavefronts. Chapter 5 presents the first images obtained with scanning SWI fluorescence microscopy. A brief conclusion reevaluates the premise of achieving nanometer resolution in x-ray microscopy.

Chapter 2

Image formation in the scanning standing-wave illumination fluorescence microscope

---

Abstract

We propose and examine image formation in the scanning standing-wave illumination (SWI) fluorescence microscope. Image formation can be characterized by a point-spread function (PSF), enabling the insights and tools of conventional imaging theory to be applied. The PSF is the product of the SWI pattern and the incoherent objective-lens PSF. The optical transfer function (OTF) is the autocorrelation of the SWI angular spectrum convolved with the objective-lens OTF. The OTF is well-suited to Fourier analysis and is readily analyzed with a graphical method. The spatial frequency cut-off is determined by the sum of the SWI numerical aperture (NA) and the objective-lens NA. The number of plane waves required for unambiguous imaging is dependent on the ratio of SWI NA to objective-lens NA. The imaging properties of the microscope can be improved by optimization of wave-vector distribution. The effects of plane-wave polarization are pronounced at high NA but are straightforward to codify. We propose that the development of the scanning SWI fluorescence microscope may enable the use of large numbers of plane waves. Con-

sequently, sub-wavelength resolution can be achieved without the need for high-NA optics.

2.1 Introduction

Resolution in wide-field fluorescence microscopy can be improved using standing-wave illumination (SWI) generated by the interference of mutually coherent plane waves. The concept was first demonstrated with the standing-wave microscope in 1993 when an improvement in axial resolution was reported using SWI generated by two counterpropagating laser beams [7]. Since then, the physical principle has been put on solid theoretical footing and demonstrated experimentally in numerous configurations. Three-dimensional (3D) improvement of both axial and lateral resolution has been demonstrated with the structured illumination microscope [8, 9, 10, 13] which uses a diffraction grating in the illumination path of a conventional fluorescence microscope. Two-dimensional (2-D) improvement of lateral resolution has been demonstrated with the harmonic excitation light microscope [14, 15] which uses as many as two pairs of off-axis laser beams. The standing-wave microscope has also undergone numerous refinements [33, 34, 35]. Improvement of lateral resolution using large numbers of plane waves has also been proposed [11, 18, 19]. Furthermore, resolution beyond the conventional diffraction limit can be achieved with the proposed standing-wave total internal reflection microscope [12, 16] which uses evanescent SWI generated by a pair of laser beams at the surface of a high-index prism.

Current SWI microscopes acquire wide-field images. Multiple wide-field images are required to generate a single post-processed image with improved resolution, and the SWI pattern must be varied in a particular manner between each image acquisition. It is not widely recognized, however, that there are unique advantages to imaging with SWI in the scanning mode rather than in the wide-field mode. The foremost of these advantages, we believe, is that the SWI pattern can be stationary throughout the image formation process. The complexity of controlling large numbers of plane waves largely limits the development of SWI microscopes with more than

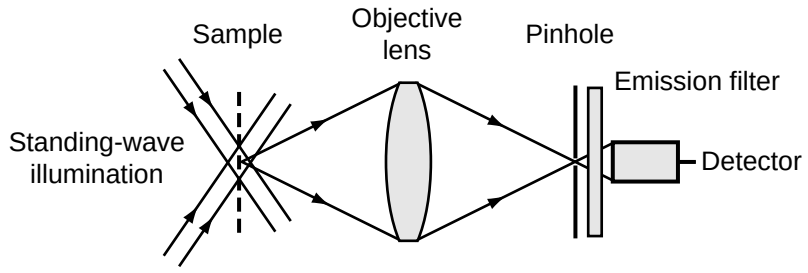

Figure 2-1: Schematic diagram of the scanning SWI fluorescence microscope. An object is illuminated by a stationary standing wave generated by the interference of multiple plane waves. As the object is scanned, light is collected by an objective lens and measured by a point intensity detector.

two pairs of plane waves. The scanning SWI microscope may enable the development of SWI microscopes with large numbers of plane waves.

In this manuscript, we examine image formation in the scanning SWI fluorescence microscope. We show that image formation can be described by a conventional point-spread function (PSF) and consider the effects of varying the number, wave-vector distribution, and polarization of the SWI plane waves. We demonstrate that scanning SWI fluorescence microscopes with large numbers of plane waves can achieve sub-wavelength resolution without the need for high-numerical-aperture (NA) optics.

2.2 Point-Spread Function

A schematic diagram of the proposed scanning SWI fluorescence microscope is shown in Fig. 1. The microscope can be analyzed as a Type 2 scanning fluorescence microscope where the illumination objective lens has been replaced by SWI [36]. Image formation in a scanning SWI fluorescence microscope can be characterized by a PSF as follows.

Let $o(\mathbf{r})$ represent the fluorophore distribution in an unknown object and $s(\mathbf{r})$ represent the SWI pattern. Assuming that fluorescence excitation is proportional to $s(\mathbf{r})$ and that fluoresced light is incoherently emitted in all directions, the pattern of

fluoresced light $i(\mathbf{r})$ at the image plane of the objective lens can be written

$$i(\mathbf{r}) = [o(\mathbf{r})s(\mathbf{r})] \otimes h_1(\mathbf{r}), \tag{2.1}$$

where $\mathbf{r}$ is a 3-D position vector (i.e., $\mathbf{r} = \hat{\mathbf{x}}x + \hat{\mathbf{y}}y + \hat{\mathbf{z}}z$), $\otimes$ denotes 3-D convolution, and $h_1(\mathbf{r})$ is the incoherent 3-D PSF of the objective lens. Unit magnification has been adopted for convenience. If the object is translated (e.g., via a scanning stage) to location $\mathbf{r}_s$, the image becomes

$$i(\mathbf{r}, \mathbf{r}_s) = [o(\mathbf{r} - \mathbf{r}_s)s(\mathbf{r})] \otimes h_1(\mathbf{r}). \tag{2.2}$$

If light is detected at only a single point $\mathbf{r} = 0$ in the image plane, the detected intensity is a function of $\mathbf{r}_s$ alone:

$$\begin{aligned} i_s(\mathbf{r}_s) &= i(\mathbf{r}, \mathbf{r}_s)|_{\mathbf{r}=0} & (2.3)\\ &= [o(\mathbf{r} - \mathbf{r}_s)s(\mathbf{r})] \otimes h_1(\mathbf{r})|_{\mathbf{r}=0}. & (2.4) \end{aligned}$$

Expanding the convolution explicitly,

$$\begin{aligned} i_s(\mathbf{r}_s) &= \int_{\boldsymbol{\rho}} o(\boldsymbol{\rho} - \mathbf{r}_s)s(\boldsymbol{\rho})h_1(\mathbf{r} - \boldsymbol{\rho})d\boldsymbol{\rho}|_{\mathbf{r}=0} & (2.5)\\ &= \int_{\boldsymbol{\rho}} o(\boldsymbol{\rho} - \mathbf{r}_s)s(\boldsymbol{\rho})h_1(-\boldsymbol{\rho})d\boldsymbol{\rho} & (2.6)\\ &= o(-\mathbf{r}_s) \otimes [s(\mathbf{r}_s)h_1(-\mathbf{r}_s)]. & (2.7) \end{aligned}$$

Replacing $o(-\mathbf{r}_s)$ with a unit impulse, we conclude that the PSF $h(\mathbf{r})$ of the scanning SWI fluorescence microscope is the *product* of the SWI pattern and the PSF of the objective lens:

$$h(\mathbf{r}) = s(\mathbf{r})h_1(-\mathbf{r}). \tag{2.8}$$

Let us now consider the SWI pattern $s(\mathbf{r})$. The standing wave generated by N

electromagnetic plane waves of identical temporal frequency can be written

$$\mathbf{E}(\mathbf{r}) = \sum_{n=1}^{N} \mathbf{E}_n \exp(j\mathbf{k}_n \cdot \mathbf{r}), \tag{2.9}$$

where $\mathbf{E}_n$ and $\mathbf{k}_n$ denote the complex electric-field vector and wave vector of the nth plane wave, respectively. Assuming that fluorescence excitation is proportional to time-averaged stored electric energy density, the SWI pattern $s(\mathbf{r})$ can be related to the standing wave by

$$\begin{aligned} s(\mathbf{r}) &= \left\langle \|\mathbf{E}(\mathbf{r},t)\|^2 \right\rangle & (2.10)\\ &= \frac{1}{2}\Re\left\{\mathbf{E}(\mathbf{r}) \cdot \mathbf{E}^*(\mathbf{r})\right\} & (2.11)\\ &= \frac{1}{2}\Re\left\{\left[\sum_{n=1}^{N} \mathbf{E}_n \exp(j\mathbf{k}_n \cdot \mathbf{r})\right] \cdot \left[\sum_{n=1}^{N} \mathbf{E}_n \exp(j\mathbf{k}_n \cdot \mathbf{r})\right]^*\right\}, & (2.12) \end{aligned}$$

where $\langle\cdot\rangle$ denotes time-averaging, $\|\cdot\|$ denotes length, $\Re\{\cdot\}$ denotes "the real part of," and * denotes complex conjugate. Since only the cross terms produce interference, $s(\mathbf{r})$ can be written as an offset plus the double summation of ${}_NC_2$ interference terms,

$$\begin{aligned} s(\mathbf{r}) &= \frac{1}{2}\Re\left\{\sum_{n=1}^{N} \mathbf{E}_n \cdot \mathbf{E}_n^* + \sum_{m=1}^{N-1}\sum_{n=m+1}^{N} \{\mathbf{E}_m \cdot \mathbf{E}_n^* \exp[j(\mathbf{k}_m - \mathbf{k}_n)\cdot\mathbf{r}]\right.\\ &\qquad \left. + \mathbf{E}_m^* \cdot \mathbf{E}_n \exp[-j(\mathbf{k}_m - \mathbf{k}_n)\cdot\mathbf{r}]\}\right\}. \end{aligned} \tag{2.13}$$

Recognizing the two terms in the double summation as complex conjugates,

$$\begin{aligned} s(\mathbf{r}) &= \frac{1}{2}\Re\left\{\sum_{n=1}^{N} \mathbf{E}_n \cdot \mathbf{E}_n^* + \sum_{m=1}^{N-1}\sum_{n=m+1}^{N} 2\Re\{\mathbf{E}_m \cdot \mathbf{E}_n^* \exp[j(\mathbf{k}_m - \mathbf{k}_n)\cdot\mathbf{r}]\}\right\} & (2.14)\\ &= \sum_{n=1}^{N} \frac{\|\mathbf{E}_n\|^2}{2} + \sum_{m=1}^{N-1}\sum_{n=m+1}^{N} |\mathbf{E}_m| \cdot |\mathbf{E}_n| \cos[(\mathbf{k}_m - \mathbf{k}_n)\cdot\mathbf{r} + (\phi_m - \phi_n)] & (2.15) \end{aligned}$$

where $|\cdot|$ denotes magnitude (i.e., complex modulus), and ϕ_n is the phase of the nth

plane wave. Combining Eq. 8 and Eq. 15, the PSF is

$$h(\mathbf{r}) = \left\{ \sum_{n=1}^{N} \frac{\|\mathbf{E}_n\|^2}{2} + \sum_{m=1}^{N-1} \sum_{n=m+1}^{N} |\mathbf{E}_m| \cdot |\mathbf{E}_n| \cos[(\mathbf{k}_m - \mathbf{k}_n) \cdot \mathbf{r} + (\phi_m - \phi_n)] \right\} h_1(-\mathbf{r}). \tag{2.16}$$

2.3 Optical Transfer Function

The OTF $H(\mathbf{f})$ of the scanning SWI fluorescence microscope is the Fourier transform of the PSF:

$$H(\mathbf{f}) = \mathcal{F}\{h(\mathbf{r})\}, \tag{2.17}$$

where $\mathbf{f}$ is a 3-D spatial-frequency vector, (i.e., $\mathbf{f} = \hat{\mathbf{x}} f_x + \hat{\mathbf{y}} f_y + \hat{\mathbf{z}} f_z$), and $\mathcal{F}$ denotes the 3-D Fourier transform. Substituting Eq. 8 and Eq. 11 and applying the convolution theorem,

$$\begin{aligned} H(\mathbf{f}) &= \mathcal{F}\left\{s(\mathbf{r})\right\} \otimes \mathcal{F}\{h_1(-\mathbf{r})\} && (2.18) \\ &= \mathcal{F}\left\{\frac{1}{2}\Re\left\{\mathbf{E}(\mathbf{r}) \cdot \mathbf{E}^*(\mathbf{r})\right\}\right\} \otimes \mathcal{F}\{h_1(-\mathbf{r})\}. && (2.19) \end{aligned}$$

Since we have shown in Eq. 15 that $\mathbf{E}(\mathbf{r}) \cdot \mathbf{E}^*(\mathbf{r})$ is purely real, we can neglect the $\Re\{\cdot\}$ operator in Eq. 19:

$$H(\mathbf{f}) = \frac{1}{2}\mathcal{F}\left\{\mathbf{E}(\mathbf{r}) \cdot \mathbf{E}^*(\mathbf{r})\right\} \otimes \mathcal{F}\{h_1(-\mathbf{r})\}. \tag{2.20}$$

Applying the Wiener-Khinchin theorem generalized to vector quantities,

$$H(\mathbf{f}) = \frac{1}{2}\left[\mathcal{F}\left\{\mathbf{E}(\mathbf{r})\right\} \star \mathcal{F}\left\{\mathbf{E}(\mathbf{r})\right\}\right] \otimes \mathcal{F}\{h_1(-\mathbf{r})\}, \tag{2.21}$$

where $\star$ denotes 3-D cross-correlation. The OTF of the microscope is the autocorrelation of the SWI angular spectrum convolved with the OTF of the objective lens. Since $\mathbf{E}(\mathbf{r})$ is a summation of plane waves, $\mathcal{F}\left\{\mathbf{E}(\mathbf{r})\right\}$ is a summation of impulses;

substituting for $\mathcal{F}\{\mathbf{E}(\mathbf{r})\}$,

$$H(\mathbf{f}) = \frac{1}{2}\left\{\left[\sum_{n=1}^{N}\mathbf{E}_n\delta(\mathbf{f}-\mathbf{k}_n)\right]\star\left[\sum_{n=1}^{N}\mathbf{E}_n\delta(\mathbf{f}-\mathbf{k}_n)\right]\right\}\otimes\mathcal{F}\{h_1(-\mathbf{r})\}. \tag{2.22}$$

2.4 Effects of Standing-Wave Illumination on Image Formation

Figure 2 illustrates the effects of SWI on image formation in the scanning SWI fluorescence microscope. The panels of Fig. 2 are explored in detail in the following sections. For simplicity, our analysis is now restricted to two dimensions (i.e., $\mathbf{r} = \hat{\mathbf{x}}x + \hat{\mathbf{y}}y$) unless otherwise noted. The amplitudes and wavelengths of all the SWI plane waves are equal, and phases are equal at the center of each PSF. The objective lens is represented by a diffraction-limited incoherent imaging system with a circular pupil function:

$$h_1(\mathbf{r}) = \left[\frac{J_1(2\pi wr)}{\pi wr}\right]^2, \tag{2.23}$$

where $r = \|\mathbf{r}\|$, J_1 is the first-order Bessel function of the first kind, and $w = \mathrm{N}A/\lambda_{em}$ [37]. Again for simplicity, the wavelength of the fluoresced light λ_{em} is assumed to be identical to the wavelength of the SWI λ. (A large difference between excitation and emission wavelengths simply scales $h_1(\mathbf{r})$ by the ratio of the two wavelengths.)

2.4.1 Number of Plane Waves

The PSF of the microscope is the product of the SWI pattern and the PSF of the objective lens (Eq. 8). In each SWI microscope shown in Fig. 2, the NA of the SWI is 0.95 (i.e., each SWI wave vector forms a 72-degree angle with the optical axis), and the NA of the objective lens is 0.10. Thus, the objective-lens PSF $h_1(\mathbf{r})$ can be interpreted as a window function in the overall PSF $h(\mathbf{r})$.

The first row of Fig. 2 shows the PSF of a SWI microscope with 15 plane waves. The 15-plane-wave PSF can be described qualitatively as a circularly symmetric function surrounded by a ring of 30 "artifacts." Inside the artifact ring, the 15-plane-wave

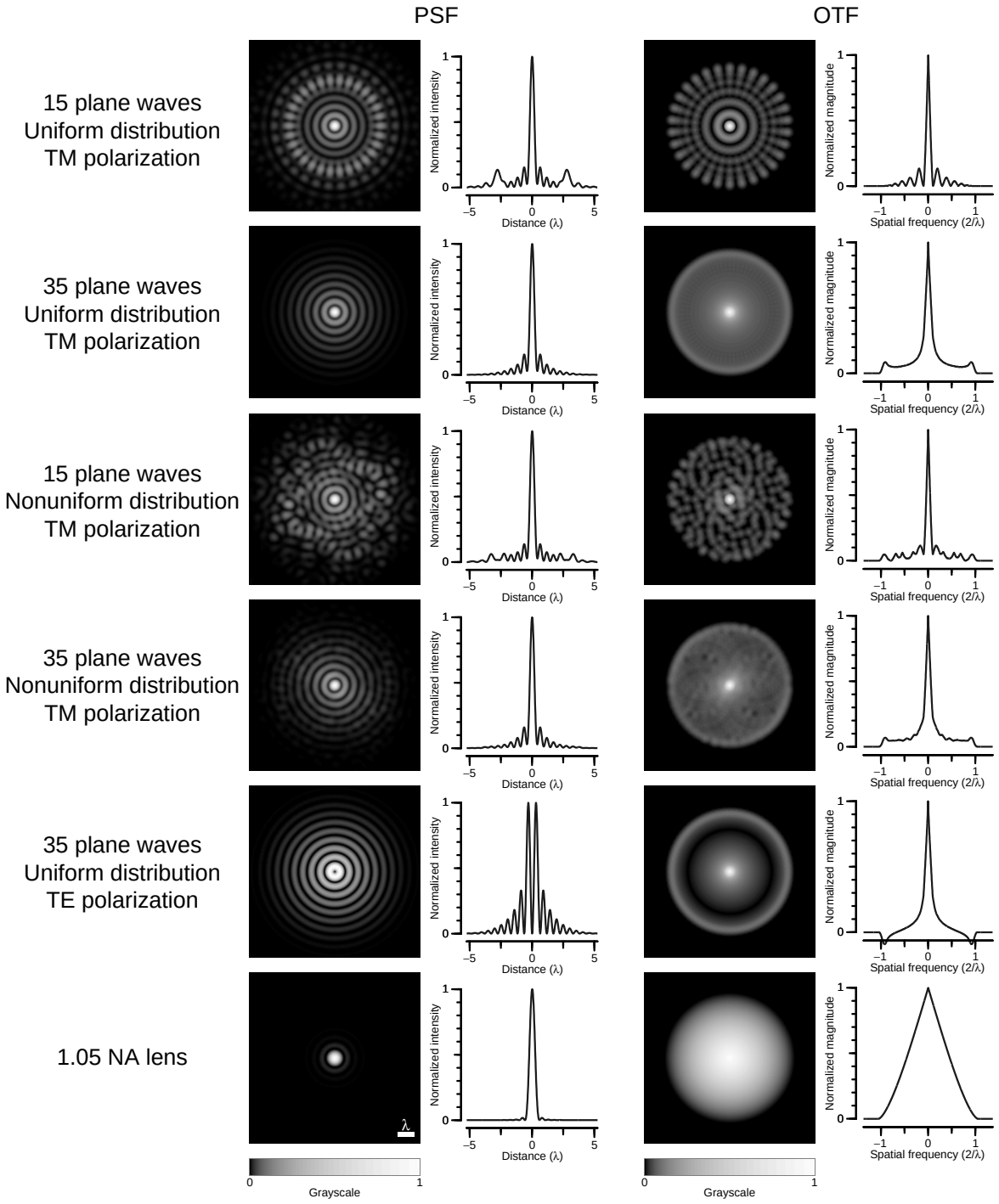

Figure 2-2: Comparison of PSFs and OTFs of several scanning SWI fluorescence microscopes. The left panels show 2-D PSFs with adjacent plots indicating the intensity values through the center of each PSF. The right panels show corresponding OTF magnitudes with adjacent plots indicating the signed magnitudes through the center of each OTF. Grayscale is proportional to the logarithm of intensity to show low-intensity features. All SWI microscopes feature 0.95 NA SWI and a 0.10 NA objective lens. A 1.05 NA objective lens (without SWI) is included for comparison.

PSF is nearly identical to the PSF of a microscope with an "infinite" number of plane waves (i.e., the microscope PSF as the number of plane waves approaches ∞). If the number of plane waves is varied, the number of artifacts in the ring remains twice the number of plane waves, and the diameter of the artifact ring is linearly proportional to the number of plane waves. The diameter of the 15-plane-wave artifact ring is approximately equal to the full-width at half-maximum intensity (FWHM) diameter of the objective-lens PSF $h_1(\mathbf{r})$.

The second row of Fig. 2 shows the PSF of a SWI microscope with 35 plane waves. Due to the windowing property of the objective-lens PSF $h_1(\mathbf{r})$, the 35-plane-wave PSF is qualitatively indistinguishable from the PSF of a microscope with an infinite number of plane waves. The diameter of the 35-plane-wave artifact ring is approximately equal to the diameter of the first zero ring of the objective-lens PSF $h_1(\mathbf{r})$.

The OTF of the microscope is the autocorrelation of the SWI angular spectrum convolved with the OTF of the objective lens (Eq. 21). Figure 3 shows a graphical analysis of the OTF which lends much insight into the imaging properties of the microscope. For example, we see that the spatial frequency cut-off of the microscope (i.e., the highest spatial frequency collected by the microscope) is determined by the sum of the SWI NA and the objective-lens NA. (For this reason, the response of a 1.05 NA objective lens without SWI is included in Fig. 2 for comparison.) The origin of the $2N$-fold symmetry in the PSF, where N is the number of plane waves, is clearly evident. Each of the SWI OTFs in Fig. 2 features a large "spike" at zero spatial frequency—the maximum at zero is a well-understood property of the autocorrelation function. We see that the autocorrelation of the SWI angular spectrum consists of as many as $1 + {}_N C_2$ impulses (which is on the order of N^2) so that the "sample" density of 2-D spatial-frequency is linearly proportional to the number of plane waves. This sampling interpretation is consistent with the observed linear relation between the diameter of the artifact ring in the PSF and the number of plane waves. Also, the roles of the SWI and of the objective lens are clearly distinguished: The SWI angular spectrum modulates copies of the objective-lens OTF to high spatial-frequency regions

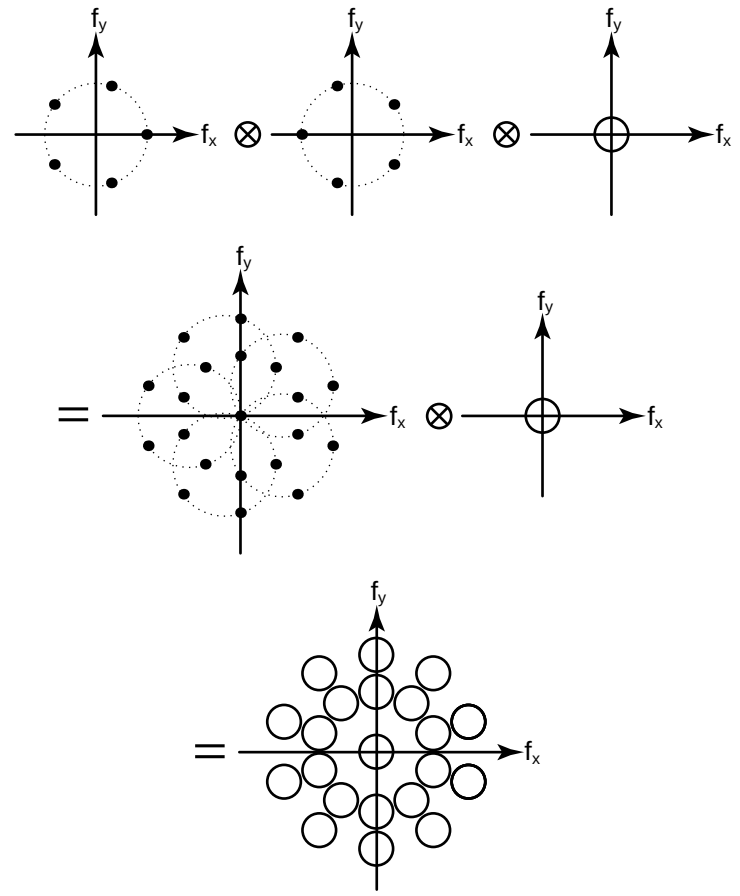

Figure 2-3: Graphical method for analyzing OTF. The top line is a graphical representation of Eq. 22 with SWI generated by five plane waves (dotted lines have been added to aid in visualization). The resulting OTF is the autocorrelation of the SWI angular spectrum convolved with the OTF of the objective lens.

of the overall OTF. Therefore, the SWI angular spectrum determines the shape of the overall OTF, while the objective-lens OTF plays the secondary role of "filling-in" the gaps in the overall OTF.

The first row of Fig. 2 shows the OTF of a SWI microscope with 15 plane waves. A minimum of 15 plane waves is required to achieve a contiguous OTF (i.e., an OTF that is non-zero throughout the entire passband). Interestingly, a minimum of 15 plane waves is also required to make the diameter of the artifact ring in the PSF exceed the FWHM diameter of the objective-lens PSF $h_1(\mathbf{r})$. An intuitive explanation for the coinciding of the two conditions in space and frequency is not yet known.

The second row of Fig. 2 shows the OTF of a SWI microscope with 35 plane

waves. The 35-plane-wave OTF is qualitatively indistinguishable from the OTF of a microscope with an infinite number of plane waves. The OTF is both contiguous and generally strong throughout the entire passband.

It was recently showed that the OTF of a microscope must be both "contiguous and generally strong" throughout the entire passband for unambiguous imaging [38]. These conditions are intimated by the PSFs and OTFs in Fig. 2 with 15 and 35 plane waves. Although the 15-plane-wave OTF is contiguous, the corresponding PSF contains a ring of artifacts. In contrast, the 35 plane-wave OTF is both contiguous and generally strong, and the corresponding PSF is qualitatively indistinguishable from the PSF of a microscope with an infinite number of plane waves. Thus, the requirement that the OTF be both contiguous and generally strong manifests itself in the SWI microscope as a lower bound on the number of plane waves required for unambiguous imaging. To first order, the required number of plane waves is linearly proportional to the ratio of SWI NA to objective-lens NA.

2.4.2 Distribution of Wave Vectors

The left side of Fig. 4 shows the autocorrelation of the SWI angular spectrum with 15 and 35 plane waves. The waves vectors are distributed uniformly around a circle so that the angular spacing between adjacent wave vectors is $2\pi/N$ radians, where N is the number of plane waves. (Recall that in our analysis all the wave vectors are equal length and form a 72-degree angle with the optical axis. Consequently, each wave vector retains only one degree of freedom). Close inspection of the Fig. 4 reveals that uniform wave-vector distributions produce highly *non*-uniform distributions of impulses after the autocorrelation. Specifically, low spatial frequencies are undersampled angularly and oversampled radially. Inversely, high spatial frequencies are undersampled radially and oversampled angularly. One could conjecture that the imaging properties of the microscope could be improved if more uniform distributions of impulses could be generated after the autocorrelation. Interestingly, a nearly identical mathematical problem is posed in the context of radio-array astronomy.

The instantaneous OTF of a radio antenna-array cross-correlation interferometer

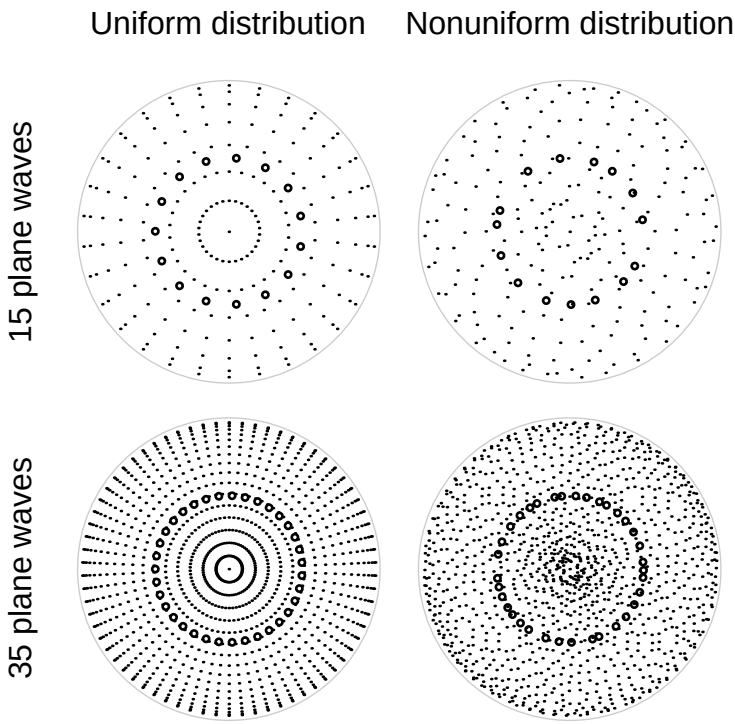

Figure 2-4: Effects of wave-vector distribution on sampling of spatial frequency with 15 and 35 plane waves. Small circles represent wave vectors, and dots represent the autocorrelation of the wave vectors.

can be described as the autocorrelation of the locations of the individual antennas [39]. Consequently, the instantaneous OTF contains gaps, necessitating the use of nonlinear image deconvolution. As in the case of the SWI microscope, one goal in the design of a radio antenna-array is a uniform distribution of impulses after an autocorrelation. However, because the autocorrelation function is not invertible in general, heuristic search algorithms are required to solve the surprisingly complex problem of minimizing the gaps in the OTF. The right side of Fig. 4 shows the autocorrelation of the SWI angular spectrum using nonuniform wave-vector distributions obtained using an elastic net algorithm adapted from analogous radio antenna-array work [40]. The corresponding PSFs and OTFs are shown in the third and fourth rows of Fig. 2.

2.4.3 Polarization

The two left images in Fig. 5 show SWI patterns generated by two sets of plane waves that are identical in all respects except for polarization. The effects of polarization

are clearly pronounced in the SWI patterns and must be taken into consideration. In contrast, the incoherent objective-lens PSF $h_1(\mathbf{r})$ is accurately described by scalar wave theory since the NA is low (0.10). Therefore, the effects of polarization on image formation can be characterized by considering the effects of SWI polarization.

We can study SWI polarization by decomposing each plane wave into two complementary linear polarizations: Transverse-magnetic (TM) polarization (also referred to as p polarization) and transverse-electric (TE) polarization (also referred to as s polarization). With TM-polarized plane waves, the relative alignment of electric-field vectors is dependent on NA. In the top left panel of Fig. 5, we see that the electric-field vectors of counterpropagating pairs of plane waves are nearly orthogonal with an NA of 0.71 in air. As a result, high spatial-frequency components in the SWI pattern are severely attenuated. In contrast, we see in the top right panel of Fig. 5 that the electric-field vectors of all the plane waves nearly parallel with an NA of 0.95 in air. In the extreme case with an NA equal to the refractive index, the electric-field vectors of all the plane waves are exactly parallel, and polarization can be neglected altogether.

With TE-polarized plane waves, the relative alignment of the electric-field vectors is independent of NA. Thus, the SWI patterns in the two bottom panels of Fig. 5 are identical with the exception of a $1/\mathrm{N}A$ spatial scaling factor. Interestingly, destructive interference occurs at the point where the phases of all the plane waves are equal. This occurs because the electric-field vectors of counterpropagating pairs of plane waves are nearly parallel but *opposite* in direction [41, 42]. With TE-polarized plane waves, SWI patterns cannot be predicted using scalar wave theory.

The first four rows of Fig. 2 show the PSFs and OTFs of microscopes with TM-polarized plane waves, while the fifth row of Fig. 2 shows the PSF and OTF of a microscope with TE-polarized plane waves. With TM polarization, each PSF features constructive interference at the point where the phases of all the plane waves are equal (i.e., at the center of the image). The OTFs are nonnegative and do not contain zeros in the passbands. With TE polarization, the PSF features destructive interference where the phases of all the plane waves are equal. The OTF is positive for high

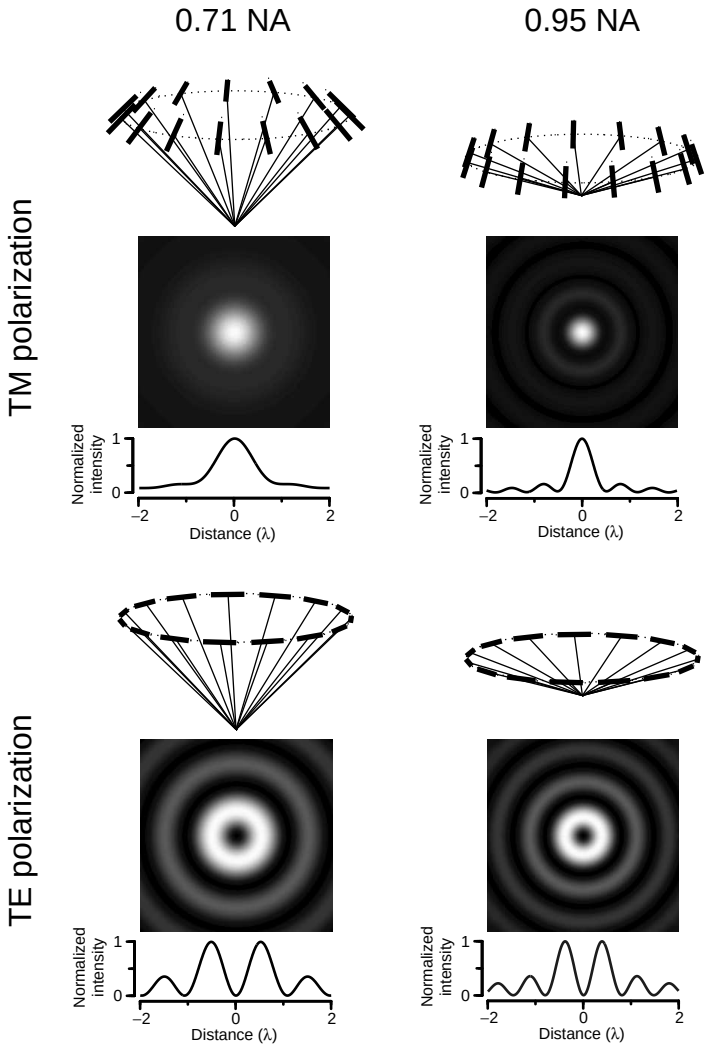

Figure 2-5: Effects of polarization on high-NA SWI patterns. The four images show calculated SWI patterns generated by four sets of plane waves that are identical in all respects except for polarization and NA. The illustrations above the images show the arrangement of wave vectors (thin lines) and electric-field vectors (thick lines) in the sets of plane waves. Wave vectors are arranged along the surface of imaginary circular cones (dotted lines have been added to aid in 3-D visualization). The plots below the images show the intensities through the center of each image.

spatial frequencies and negative for low spatial frequencies. A zero ring occurs at spatial frequencies corresponding to pairs of plane waves with orthogonal electric-field vectors.

2.5 Image Evaluation

Figure 6 shows numerically simulated images generated by the SWI microscopes shown in Fig. 2. Images were calculated by convolving a test object with the PSFs. The grayscale test object consists of four sections: A single layer of $\lambda/2$-diameter spheres, a nested elbow pattern with $\lambda/4$-width lines and spaces, a mesh of thin lines of various widths, and a pattern of line segments. Poisson noise was generated to simulate photon counting statistics at low light levels. The photon counts along the top of Fig. 6 indicate the maximum number of expected photons per pixel with a simulated pixel size of $(\lambda/8)^2$. Images were then linearly filtered by the approximate inverse of each OTF:

$$H^{-1}(\mathbf{f}) \approx \frac{H^*(\mathbf{f})}{|H(\mathbf{f})|^2 + \mu}, \tag{2.24}$$

where μ is a regularization parameter [43]. In each image, μ was set to the value that minimized the mean squared error.

The top row of Fig. 6 shows images generated by a microscope with 15 plane waves, which is the minimum number of plane waves required to achieve a contiguous OTF with 0.95 NA SWI and a 0.10 NA objective lens. The second row of Fig. 6 shows images generated by a microscope with 35 plane waves. Even though the OTFs of both microscopes are contiguous, we see that the 35-plane-wave images contain less noise than the 15-plane-wave images. This echoes the recent report that the OTF of a microscope must be both "contiguous and generally strong" for unambiguous imaging [38]. We also see that the effects of the artifact ring in the 15-plane-wave PSF are difficult to remove from images, even with 10000 photons per pixel. In contrast, the 35-plane-wave PSF does not contain an artifact ring.

The third and fourth rows of Fig. 6 show images generated by microscopes with nonuniform wave-vector distributions. With a nonuniform distribution, we see that

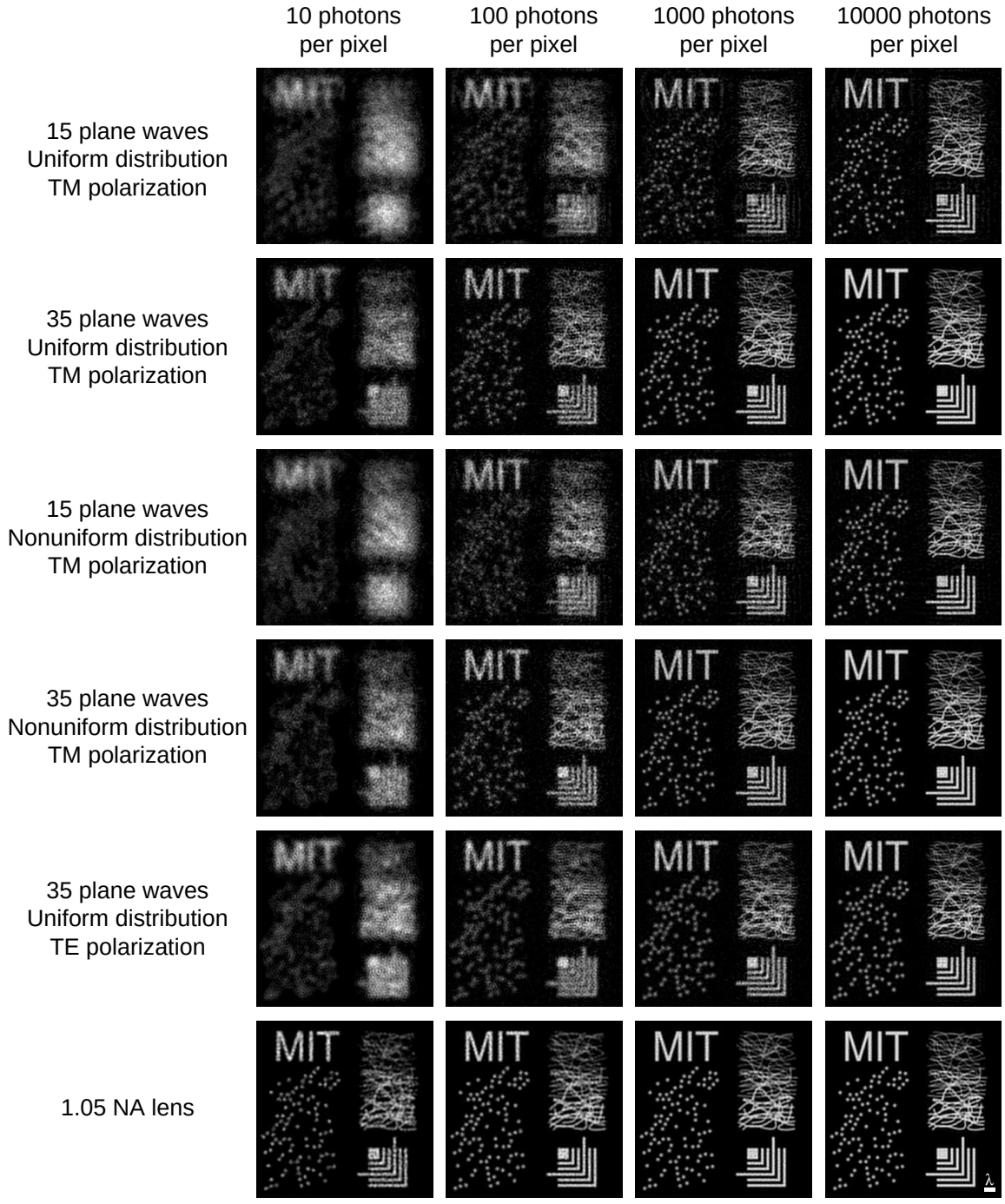

Figure 2-6: Comparison of numerically simulated images generated by several scanning SWI fluorescence microscopes. Images were calculated by convolving a test object with the PSFs of the microscopes shown in Fig. 2. Poisson noise was generated to simulate low photon counts. Images were then inverse filtered to facilitate visual comparison.

the effects of the artifact ring in the 15-plane-wave images are reduced. However, the 15-plane-wave images contain more noise than the 35-plane-wave images. With 35 plane waves, images with nonuniform and uniform wave-vector distributions are nearly indistinguishable. Close examination of the 35-plane-wave images reveals that the images with nonuniform wave-vector distribution contain slightly more noise than the images with uniform wave-vector distribution.

The fifth row of Fig. 6 shows images generated by a microscope with TE-polarized plane waves. Although the microscope features a destructive PSF (i.e., destructive interference occurs at the point where the phases of all the plane waves are equal), the effects are largely removed by the inverse filtering. The near-equivalence of imaging with constructive and destructive PSFs has been explored experimentally in the context of 4Pi confocal fluorescence microscopy [44].

The last row of Fig. 6 shows images generated by a 1.05 NA objective lens without SWI. A 1.05 NA objective lens was selected for comparison because the spatial frequency cut-off of the SWI microscope is determined by the sum of the SWI NA (0.95) and the objective-lens NA (0.10). The non-SWI images contain significantly less noise than the SWI images. This can be attributed to the "spike" at zero frequency in SWI OTFs.

2.6 Discussion

The effects of plane-wave phase have been neglected in this manuscript; the phases of all the plane waves have simply been set equal at the center of the PSF. However, we have found that the condition that the OTF is generally strong throughout the passband depends critically on the alignment of the plane-wave phases. Furthermore, we have found that aligning the phases of the plane waves is perhaps the most challenging aspect of constructing scanning SWI fluorescence microscopes with large numbers of plane waves. The relation between plane-wave phase and signal-to-noise in SWI images has been studied in the context of the standing-wave total internal reflection microscope [16]. Also, a method for retrieving an unknown phase difference between

a pair of coherent counterpropagating wave fronts directly from acquired images has been demonstrated [45]. We are currently preparing a manuscript devoted to examining the effects of plane-wave phase on imaging in the scanning SWI fluorescence microscope and to presenting a practicable method for aligning the phases of the plane waves.

In our study of SWI polarization, we noted that the effects of polarization could be largely neglected with TM-polarized plane waves at high NA (0.95). Consequently, it would at first appear that TM polarization is of greater practical importance than TE polarization. However, refraction of TM-polarized plane waves at the air-glass interface of a cover slip would rotate the electric-field vectors and severely attenuate high spatial-frequency components in the SWI. Consequently, TE polarization may be of greater practical importance because coupling prisms and the like are not required to preserve high spatial-frequency components in the SWI.

The analyses in sections 2 and 3 were performed in three dimensions, while the analyses in the following sections were formed in two dimensions for simplicity. Extension of the 2-D results to three dimensions appears straightforward. However, at least one important result does not scale to three dimensions: The number of plane waves required to satisfy the condition that the OTF is both contiguous and generally strong is no longer linearly proportional to the ratio of SWI NA to objective-lens NA. This occurs because the number of impulses after the autocorrelation remains on the order of N^2 ($1 + {}_NC_2$, where N is the number of plane waves), while maintaining a given sample density in 3-D spatial-frequency requires a number of samples on the order of N^3.

One author has commented on the "technical complexity of controlling the interference patterns" of a SWI microscope with just four plane waves [38]. We are currently completing a prototype scanning SWI fluorescence microscope with a large number of plane waves, and we concur with the notion. We believe however that the capability of achieving sub-wavelength resolution without high-NA optics may justify the increase in complexity.

2.7 Conclusion

The development of the scanning SWI fluorescence microscope could potentially provide new approaches to solving many challenging problems in microscopy. We have shown that the effects of SWI in image formation can be completely encapsulated in a conventional PSF, enabling the insights and tools of conventional linear space-invariant imaging theory to be applied. The PSF is well-suited to Fourier analysis and allows for an insightful graphical method for OTF analysis. In the scanning SWI fluorescence microscope, high-NA illumination can be generated through aperture synthesis using large numbers of plane waves: Sub-wavelength resolution can be achieved with low-NA optics.

Chapter 3

Lensless patterning of light with direct angular spectrum synthesis

Abstract

X-ray microscopes have the potential to achieve nanometer resolution [46, 23]. In practice, however, the resolutions of x-ray focusing optics are limited to approximately 20 nanometers [26, 28, 47]. Several methods for improving resolution have been proposed including the use of higher diffracted orders in zone plates [28], x-ray diffraction microscopy [29], and photon sieves [30]. Here we show it is possible to pattern light with sub-wavelength resolution using the interference of a large number of modulated laser beams. With the advent of new coherent x-ray sources [48, 49, 50, 51, 52] the technique requires only an assembly of flat mirrors fabricated with macroscopic accuracy and hence is feasible at x-ray wavelengths. We envision that this technique will be useful for applications at both x-ray and optical wavelengths including microscopy, lithography, and optical trapping.

The *angular spectrum of plane waves* concept asserts that any propagating monochromatic pattern of light can be represented as a superposition of homogeneous and inhomogeneous (i.e., evanescent) plane waves [53, 54]. In the scalar approximation of electromagnetic wave theory, the directions, amplitudes, and phases of the plane

waves are related to the pattern of light by a Fourier transform. The elegance of this approach is a hallmark of Fourier optics [37]. Angular spectrum decomposition is well understood and widely used for analysis. It is not widely recognized, however, that the angular spectrum concept can also be used for synthesis: a pattern of light can be synthesized directly from its angular spectrum of plane waves.

In our experiment, we synthesized an approximation of the angular spectrum of a vector Bessel beam with azimuthal polarization [41, 55, 42] using 15 laser beams. The experimental apparatus (Fig. 1) converts the expanded linearly polarized beam of an argon ion laser ($\lambda = 488$ nm) into a converging circular cone of 15 beams with a half-angle of 72 degrees. Azimuthal polarization was achieved by aligning the electric-field vector of each beam perpendicular to the optical axis (i.e., each beam was *s*-polarized). Radial polarization could be achieved if desired by simply rotating the polarization of the single input beam by 90 degrees. Beam paths were designed with matching path lengths, and mirrors were mounted on a single aluminum plate for mechanical and thermal stability. One mirror in each beam path was mounted on a piezoelectric actuator, allowing the phase of each beam to be modulated independently. With the exception of a beam expander (not shown), the optical path consists entirely of flat mirrors.

The interference pattern generated by the apparatus was measured by projecting the cone of beams through a glass cover slip and into the oil-immersed focal plane of a $160\times$ / 1.4 NA oil-immersion microscope objective. The magnified image produced by the objective was recorded with a charge-coupled device (CCD) imager. In general, the pattern of light generated by a high numerical aperture (NA) optical system (e.g., our 0.95 NA cone of beams) cannot be measured accurately in this manner due to the effects of polarization. However, since our experiment utilized azimuthal polarization the pattern of light incident on the CCD imager was simply a magnified replica of the pattern of light at the focal plane of the objective.

While the design of the beam paths correctly sets the polarization and wave vectors of the 15 beams, generating a vector Bessel beam also requires that the amplitudes and phases of all the beams are equal at the center of the pattern. Since the trans-

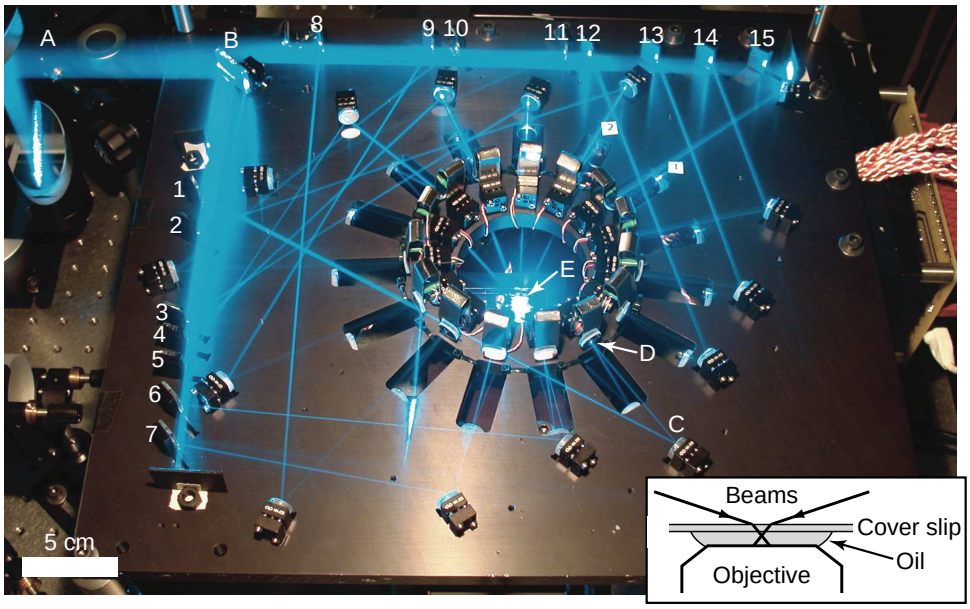

Figure 3-1: Experimental apparatus for direct angular spectrum synthesis using 15 laser beams. The expanded beam of a visible-light laser (A) is spatially chopped in half by a mirror (B), and then further chopped into 15 beams by two rows of pick-off mirrors (1-7 and 8-15). Each of the 15 beams is then directed by a subsequent mirror (C) to one of a ring of 15 mirrors (D), each mounted on a piezoelectric actuator. The actuated mirrors then direct the beams down through a ring of slots to a final ring of recessed mirrors, which direct the beams to a common region of overlap (E). In the region of overlap, the converging cone of 15 beams passes through a cover slip into immersion oil (inset illustrates cross section), where the pattern of light at the focal plane of a high-power oil-immersion objective is imaged.

verse amplitude profile of each beam was smoothly varying but non-constant, the amplitudes were matched by suitable lateral adjustments of the beams. The phases were not as straightforward to equalize, as it was not possible to measure the phases of the beams directly. Since we could measure the pattern generated by the apparatus, we developed a method for estimating the relative beam phases from an image of the pattern. Each piezoelectric phase actuator was then adjusted accordingly to equalize the phases of the beams: phase alignment was achieved and maintained in a feedback loop. In that respect, our experimental apparatus resembles an adaptive optic. However, since our approach uses coherent light, the phase of each beam could be shifted by any integer number of wavelengths with no change to the generated pattern. As a result, the fabrication tolerances of our apparatus were determined by the temporal coherence length of the laser source (meters) and not by a fraction of the wavelength of light (hundreds of nanometers).

The left panels of Fig. 2 show the predicted and measured patterns of light generated by the apparatus. The properties of the vector Bessel beam with azimuthal polarization are well known [41, 42]. The center of the pattern features an annulus approximately $\lambda/1.6$ in diameter. The null in the center of the annulus corresponds surprisingly to the point where the phases of all the beams are equal. This occurs because azimuthal polarization produces a phase singularity at that point which leads to destructive (rather than constructive) interference.

The annulus is surrounded by a ring of 30 "artifacts" approximately $15\lambda/(2\pi)$ in radius. Inside the artifact ring, the pattern of light is nearly identical to the vector Bessel beam. Outside the artifact ring lies a complex array of lobes with 30-fold symmetry. A Fourier transform reveals the underlying cause of the structure (Fig. 2, right panels). The spatial frequency spectrum of the pattern of light is a summation of impulses (i.e., a discrete function). Synthesizing an angular spectrum with a finite number of plane waves results in a "sampled" version of the continuous angular spectrum. The radius of the artifact ring is linearly proportional to the number of plane waves used in the synthesis. This result is consistent with the sampling interpretation of direct angular spectrum synthesis. In the limit as the

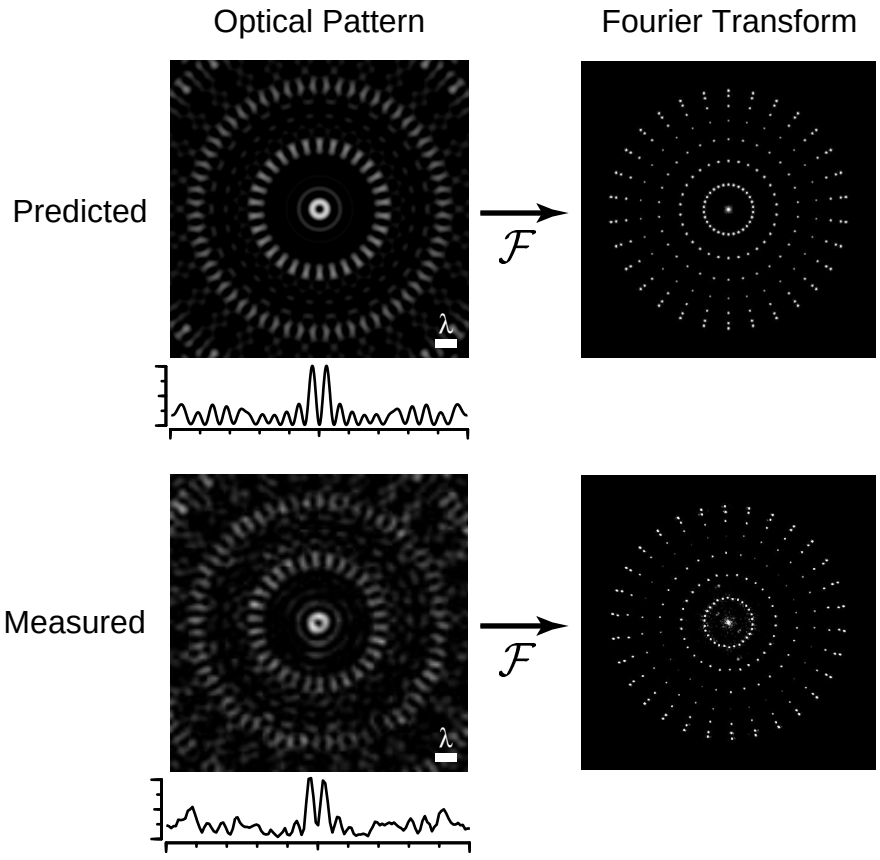

Figure 3-2: Predicted and measured patterns of light generated with direct angular spectrum synthesis. The top-left image shows the predicted pattern generated by direct angular spectrum synthesis using 15 plane waves. The bottom-left image shows the measured pattern generated by the experimental apparatus. The intensities of the center row of pixels are plotted below each image, and the Fourier transforms of the patterns are shown to the right.

number of plane waves approaches infinity, the pattern of light becomes exactly the vector Bessel beam with azimuthal polarization.

The maximum resolution attainable with direct angular spectrum synthesis is limited fundamentally by diffraction. Since evanescent waves cannot be generated by a far-field apparatus, the highest spatial frequency that can be generated is $4\pi/\lambda$. Aside from the effects of diffraction, the range of patterns that can be generated with direct angular spectrum synthesis is limited only by the number of plane waves. Generating arbitrary patterns requires a continuum of spatial frequencies. Since the superposition of plane waves is a discrete approximation of a continuous angular spectrum, in theory an infinite number of plane waves is required to generate arbitrary patterns. However, since any pattern in a *finite* region of space can be represented by a finite number of samples in frequency, in practice the number of plane waves limits only the "field of view" in which arbitrary patterns can be generated.

We expect direct angular spectrum synthesis will be important for applications at both x-ray and optical wavelengths. At x-ray wavelengths, high-NA lenses do not seem feasible in the near future. Outstanding reflective imaging systems have been developed for next-generation optical projection lithography with resolutions of less than 70 nm at $\lambda = 13$ nm [56]. However, nanometer resolution is not currently feasible due to fabrication tolerances required of the mirrors. Higher resolution can be achieved using Fresnel zone plates. However, for reasons not entirely understood, the maximum resolution of x-ray zone plates is currently limited to approximately 20 nm [26, 28]. Since direct angular spectrum synthesis requires only an assembly of mirrors fabricated with macroscopic accuracy, the technique is feasible at x-ray wavelengths. At optical wavelengths, over a century of continuous development in lens design has made the use of high-NA lens systems with diffraction-limited resolutions virtually routine. However, many challenges remain. For example, it has been shown both theoretically [57, 58] and experimentally [59, 60] that at high NA a radially-polarized beam focuses to a smaller spot than a linearly or circularly polarized beam. Unfortunately, generating and coupling a radially-polarized beam to a high-NA lens with sub-wavelength wavefront distortion is not straightforward, and a variety of

methods have been explored [59, 60, 61, 62, 63]. Although our experiment utilized azimuthal polarization, radial polarization could be produced by simply rotating the polarization of the input beam by 90 degrees. [1] In theory, this would generate a focused spot of light with a full-width at half-maximum diameter of $\lambda/2.6$, which to our knowledge represents the smallest spot ever generated in the far field. Another remaining challenge to lens design is increasing working distance: lens aberrations and fabrication tolerances limit the development of microscope objectives with both high NA and long working distance. Our experimental apparatus simultaneously achieves a NA of 0.95 in air and a working distance of 22 mm. Since direct angular spectrum synthesis is a lensless technique, it is not constrained by the conventional limitations of lens design.

Supplementary Methods

Interference patterns generated with direct angular spectrum synthesis

The standing wave generated by N electromagnetic plane waves of identical temporal frequency can be written

$$\mathbf{E}(\mathbf{r}) = \sum_{n=1}^{N} \mathbf{E}_n \exp(j\mathbf{k}_n \cdot \mathbf{r}), \tag{3.1}$$

where $\mathbf{r}$ is a 3-D position vector (i.e., $\mathbf{r} = \hat{\mathbf{x}}x + \hat{\mathbf{y}}y + \hat{\mathbf{z}}z$), and $\mathbf{E}_n$ and $\mathbf{k}_n$ denote the complex electric-field vector and wave vector of the nth plane wave, respectively. Assuming that the detected interference pattern is proportional to time-averaged electric energy density, the interference pattern $I(\mathbf{r})$ can be related to the standing wave by

$$I(\mathbf{r}) \;=\; \left\langle \|\mathbf{E}(\mathbf{r},t)\|^2 \right\rangle \tag{3.2}$$

[1] See Supplementary Notes.

$$= \frac{1}{2}\Re\left\{\mathbf{E}(\mathbf{r})\cdot\mathbf{E}^{*}(\mathbf{r})\right\} \tag{3.3}$$

$$= \sum_{n=1}^{N}\frac{\|\mathbf{E}_n\|^2}{2} + \sum_{m=1}^{N-1}\sum_{n=m+1}^{N}|\mathbf{E}_m|\cdot|\mathbf{E}_n|\cos[(\mathbf{k}_m-\mathbf{k}_n)\cdot\mathbf{r}+(\phi_m-\phi_n)], \tag{3.4}$$

where $\langle\cdot\rangle$ denotes time-averaging, $\|\cdot\|$ denotes length, $\Re\{\cdot\}$ denotes "the real part of," * denotes complex conjugate, $|\cdot|$ denotes complex modulus, and ϕ_n is the phase of the nth plane wave. The Fourier transform of $I(\mathbf{r})$ is a summation of impulses determined by the autocorrelation of the angular spectrum:

$$\mathcal{F}\{I(\mathbf{r})\} = \frac{1}{2}\left\{\left[\sum_{n=1}^{N}\mathbf{E}_n\delta(\mathbf{f}-\mathbf{k}_n)\right]\star\left[\sum_{n=1}^{N}\mathbf{E}_n\delta(\mathbf{f}-\mathbf{k}_n)\right]\right\}, \tag{3.5}$$

where $\mathcal{F}$ denotes the 3-D Fourier transform, $\mathbf{f}$ is a 3-D spatial-frequency vector (i.e., $\mathbf{f}=\hat{\mathbf{x}}f_x+\hat{\mathbf{y}}f_y+\hat{\mathbf{z}}f_z$), and $\star$ denotes 3-D cross-correlation.

The predicted interference pattern in a plane generated by the experimental apparatus with 15 plane waves is shown in the top-left panel of Fig. 2. The left and center panels of Fig. S1 show the predicted interference patterns generated by 30 and 45 plane waves, respectively. In all cases, the wave vectors form a converging circular cone with a half-angle of 72 degrees (i.e., $\mathrm{N}A = 0.95$) and are uniformly distributed in angle. Note that the artifact ring contains $2N$ artifacts arranged in a circle with a radius of approximately $N\lambda/(2\pi)$. This occurs because $\mathcal{F}\{I(\mathbf{r})\}$ consists of impulses arranged in N straight rows like the spokes of a wheel. (This is valid for N odd. A similar argument exists for N even.) Each row of impulses corresponds to collinear spatial frequencies with periods T_n given by

$$T_n = \frac{\lambda}{2\sin(n\pi/N)} \tag{3.6}$$

for $0 \le n \le N$. Due to the small-angle approximation of the sine function, the largest finite period T_1 is an approximate integer multiple of a large fraction of the collinear spatial frequencies. The resulting constructive interference generates one pair of artifacts for each of the N rows of impulses at a distance of $T_1 \approx N\lambda/(2\pi)$ from the center of the pattern.

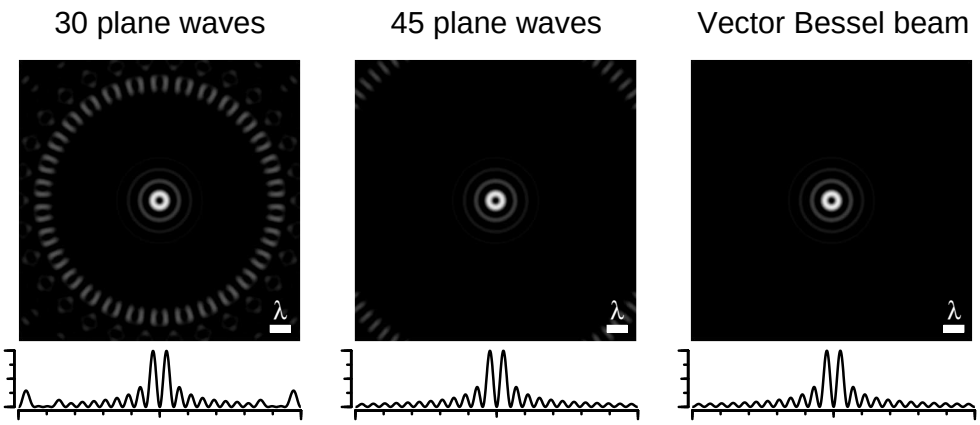

Figure 3-3: Predicted interference patterns with 30 and 45 plane waves and the vector Bessel beam with azimuthal polarization. The intensities of the center row of pixels are plotted below each image.

The pattern inside the artifact ring is nearly identical to the vector Bessel beam with azimuthal polarization (Fig. S1, right panel) given by

$$I(r) = {J_1}^2(k_r r), \tag{3.7}$$

where r is a cylindrical coordinate (i.e., $r = \sqrt{x^2 + y^2}$), J_1 is the first order Bessel function of first kind, and $k_r = \|\mathbf{k}_n\| \times \mathrm{N}A$. The intensity through the center of the annulus plotted in Fig. S2. With azimuthal polarization, the blue line shows time-averaged electric energy density, while the red line shows time-averaged magnetic density. With radial polarization, the blue line shows time-averaged *magnetic* energy density, while the red line shows time-averaged *electric* energy density. The peak-to-peak diameter of the annulus (blue line) is $\lambda/1.6$. The full-width at half-maximum diameter of the focused spot (red line) is $\lambda/2.6$, corresponding to a circular area of $0.12\lambda^2$.

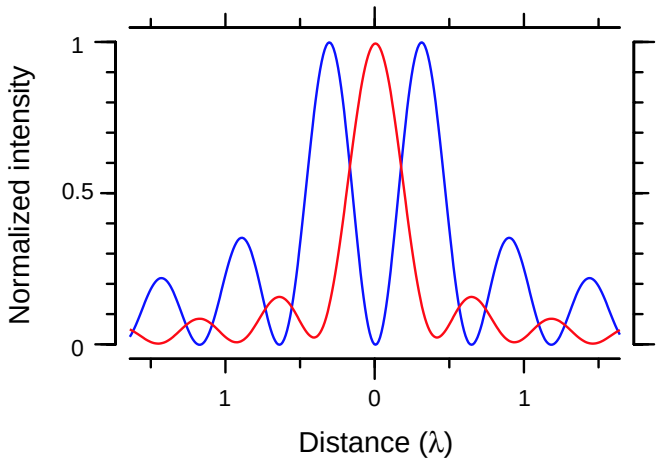

Figure 3-4: Predicted interference patterns with azimuthal polarization (blue line) and radial polarization (red line).

Retrieval of optical phase from an intensity interference pattern

The Fourier transform of $I(\mathbf{r})$ can be expressed as a summation of impulses (Eq. 5). Each impulse corresponds to a pair of plane waves (e.g., plane waves m and n); the location and complex amplitude of each impulse are given by $\mathbf{k}_m - \mathbf{k}_n$ and $\mathbf{E}_m \cdot \mathbf{E}_n^*$, respectively. If all the wave vectors $\mathbf{k}_n$ are known, the complex amplitude $\mathbf{E}_m \cdot \mathbf{E}_n^*$ for every pair of plane waves can be determined from the Fourier transform of $I(\mathbf{r})$. Subsequently, if $\mathbf{E}_m \cdot \mathbf{E}_n^*$ for every pair of plane waves is known, the complex amplitude of every the plane wave $\mathbf{E}_n$ is overdetermined. Hence, the phases of all the plane waves can be determined from an intensity image of the interference pattern $I(\mathbf{r})$.

Our method consists of three steps. The first step estimates $\mathbf{k}_n$ from $I(\mathbf{r})$ using a Fourier transform followed by a matched Hough transform. The interference pattern $I(\mathbf{r})$ is first multiplied by a circularly-symmetric raised-cosine window, and then $\mathcal{F}\{I(\mathbf{r})\}$ is calculated using the two-dimensional fast Fourier transform. The squared magnitude of $\mathcal{F}\{I(\mathbf{r})\}$ is shown on a logarithmic grayscale in the bottom-right panel of Fig. 2. Note that $\mathcal{F}\{I(\mathbf{r})\}$ was calculated using a 1024×1024-pixel region of $I(\mathbf{r})$, while the bottom-left panel of Fig. 2 shows a cropped 128×128-pixel detail.

Since the wave vectors in our experimental apparatus were arranged in a circular

cone, the angular spectrum $\sum_{n=1}^{N} \mathbf{E}_n \delta(\mathbf{f} - \mathbf{k}_n)$ consisted of impulses arranged in a circle. Since $\mathcal{F}\{I(\mathbf{r})\}$ is the autocorrelation of the angular spectrum (Eq. 5), $\mathbf{k}_n$ can be estimated using a matched Hough transform by replacing each pixel in $\mathcal{F}\{I(\mathbf{r})\}$ with the line integral around a circle centered at that pixel. The radius of the circle is approximately half the radius of the largest ring of impulses in $\mathcal{F}\{I(\mathbf{r})\}$. The matched Hough transform contains a ring of $2N$ peaks from which $\mathbf{k}_n$ can be estimated.

The second step in our method estimates $\mathbf{E}_m \cdot \mathbf{E}_n^*$ for every pair of plane waves from $\mathbf{k}_n$ (estimated in the first step) and $I(\mathbf{r})$. Since $\mathcal{F}\{I(\mathbf{r})\}$ is the autocorrelation of the angular spectrum, the impulse in $\mathcal{F}\{I(\mathbf{r})\}$ with complex amplitude $\mathbf{E}_m \cdot \mathbf{E}_n^*$ should be located at spatial frequency $\mathbf{k}_m - \mathbf{k}_n$. Since the impulses were well-resolved in $\mathcal{F}\{I(\mathbf{r})\}$ (Fig. 2, bottom-left), $\mathbf{E}_m \cdot \mathbf{E}_n^*$ was estimated as the complex value of the pixel with the largest complex modulus in the 11×11-pixel region of $\mathcal{F}\{I(\mathbf{r})\}$ centered at $\mathbf{k}_m - \mathbf{k}_n$.

Note that while Eq. 5 can be written as the sum of N^2 impulses, N of the impulses correspond to the same spatial frequency (i.e., $\mathbf{k}_m - \mathbf{k}_n = 0$ for all $m = n$). As a result, $\mathcal{F}\{I(\mathbf{r})\}$ contains at most $N^2 - N + 1$ distinct impulses corresponding to the sum of a zero-frequency term and ${}_N C_2$ interference terms.

The third step in our method estimates the complex amplitude $\mathbf{E}_n$ of every plane wave from $\mathbf{E}_m \cdot \mathbf{E}_n^*$ for every pair of plane waves (estimated in the second step). An error function can be defined as

$$E(\mathbf{X}_1..\mathbf{X}_N) = \sum_{m=1}^{N} \sum_{n=1}^{N} |\mathbf{E}_m \cdot \mathbf{E}_n^* - \mathbf{X}_m \cdot \mathbf{X}_n^*|, \tag{3.8}$$

where $\mathbf{E}_m \cdot \mathbf{E}_n^*$ are the *observed* complex amplitudes (estimated in the second step), and $\mathbf{X}_n$ is the *unknown* complex amplitude of the nth plane wave. Since N unknown amplitudes $\mathbf{X}_n$ are constrained by up to $N^2 - N + 1$ observations of $\mathbf{E}_m \cdot \mathbf{E}_n^*$, $\mathbf{X}_n$ is overdetermined and can be estimated by minimizing the error function. The initial guesses for the amplitudes, phases, and directions of $\mathbf{X}_n$ were identically unity, random with uniform distribution between 0 and 2π radians, and orthogonal to $\mathbf{k}_n$ (estimated in the first step) assuming perfect azimuthal polarization, respectively. On average,

an iterative technique developed for the minimizing the error function[3] settled to less than 0.1%-between-iterations in 4.7 iterations.

Supplementary Notes

Azimuthal polarization was utilized in our experiment because the generated pattern could be measured directly using a microscope objective and a CCD imager. The pattern generated with radial polarization could be inferred but not measured directly using this technique because the radial polarization vectors would be rotated by the objective. However, the radially-polarized pattern could be measured if desired with near-field scanning optical microscopy techniques or with a knife-edge method [64].

Chapter 4

Phase alignment for standing-wave illumination microscopy by iterative maximization of point intensity

---

Abstract

In microscopes that use the interference of large numbers of wavefronts to generate structured illumination, knowledge of the phase differences amongst the wavefronts alone is insufficient for imaging in the presence of noise. The wavefront phases must be aligned *prior* to imaging. We describe a simple technique for aligning the phases of a large number of wavefronts by iterative maximization of point intensity. We show theoretically that the iterative algorithm is guaranteed to converge monotonically and demonstrate the technique experimentally using a scanning standing-wave illumination microscope with 15 laser beams.

4.1 Introduction

In microscopes that use the interference of multiple wavefronts to generate structured illumination, knowledge of the phase differences amongst the wavefronts is critical to image formation. For example, in 4Pi-confocal microscopy, the phase difference between two spherical wavefronts is controlled by adjusting the path length of one of the interference arms [65]. If the phase difference is known, nearly identical images can be obtained whether the wavefronts are perfectly in-phase or completely out-of-phase [44, 45]. In structured illumination and harmonic excitation light microscopy [8, 9, 13, 14, 15], the phase difference between two planar wavefronts is controlled by shifting a diffraction grating in the illumination path and by modulating the phase of one of the laser beams, respectively. While the value of the initial phase difference is unimportant, knowledge of the phase difference in each pre-processed image is required to produce the final post-processed image.

In proposed microscopes that use more than one or two pairs of wavefronts, knowledge of the phase differences alone may be inadequate for imaging. For example, the recently proposed scanning standing-wave illumination (SWI) microscope could enable the use of tens or hundreds of planar wavefronts; with a sufficiently large number of planar wavefronts, SWI can be the *primary source* of resolution rather than a secondary means for resolution enhancement. In theory, sub-wavelength resolution can be achieved using only low numerical aperture (NA) optics. Fig. 1 shows the magnitude of the calculated two-dimensional optical transfer function (OTF) of a scanning SWI fluorescence microscope with illumination generated by 15 plane waves. The 15 propagation vectors are arranged in a converging circular cone with a numerical aperture (NA) of 0.95, and the NA of the objective lens is 0.20. The 15 plane waves are transverse-magnetic polarized with respect to the image plane (i.e., the SWI is radially polarized). Overall signal-to-noise is maximal with equal plane-wave phases (Fig. 1, bottom panel). In contrast, the OTF is generally lower and passes through zero in multiple places throughout the passband with random plane-wave phases (Fig. 1, top panel). In the presence of noise, the OTF with random plane-wave phases cannot

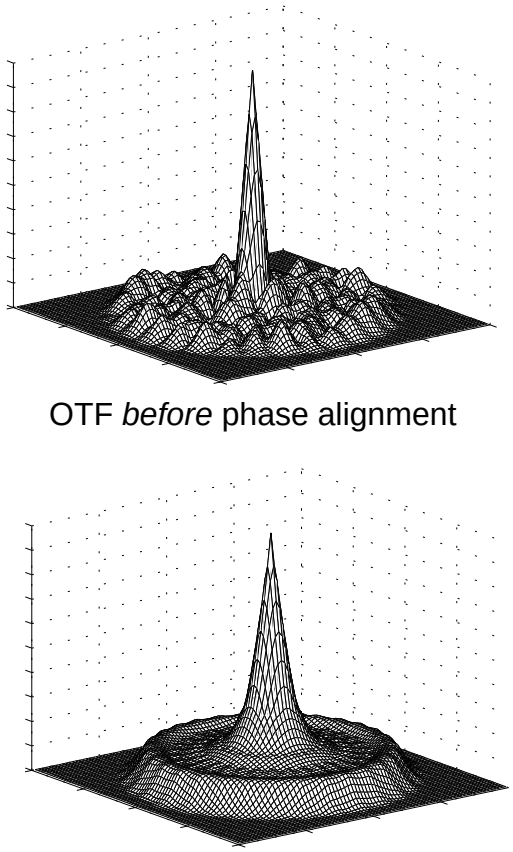

Figure 4-1: Effects of phase alignment on OTF. The two panels show the calculated OTFs of identical scanning fluorescence microscopes with SWI generated by 15 plane waves. The top panel shows the OTF with random plane-wave phases. The bottom panel shows the OTF with plane-wave phases equalized at the center of the PSF.

be computationally restored without sacrificing resolution. Knowledge of the phase differences alone is insufficient for imaging; in a scanning SWI microscope with a large number of wavefronts, the wavefront phases must be aligned *prior* to imaging.

In this manuscript, we analyze and demonstrate a technique for aligning the phases of a large number of wavefronts by iterative maximization of point intensity. The technique is well-suited for use in a scanning SWI microscope and does not require additional optical apparatus. We show theoretically that the iterative algorithm is guaranteed to converge monotonically, explore the properties of technique with numerical experiments, and demonstrate the technique experimentally by aligning

the wavefront phases of a scanning SWI microscope with 15 laser beams.

4.2 Iterative Algorithm for Phase Alignment

The task of phase alignment in a scanning SWI microscope can be described as follows. Illumination in a scanning SWI microscope is generated by the interference of multiple planar wavefronts (i.e., "plane waves"). The phase of each plane wave can be shifted independently. However, the initial phase of each plane wave is not known because the SWI apparatus contains macroscopically-positioned optical components. Consequently, the initial phases of the plane waves are essentially random. The goal of phase alignment is to appropriately shift the phase of each plane wave to equalize all the phases at the center of the point-spread function (PSF).

An iterative phase alignment algorithm is readily understood in the case of two plane waves. The interference of two plane waves produces the familiar fringe pattern (i.e., an offset sinusoidal intensity pattern). The peaks of the fringe pattern correspond to locations where the plane waves are equal in phase, while the valleys of the fringe pattern correspond to locations where the plane waves are π radians out of phase. The positions of the peaks and valleys are determined by the difference in phase between the plane waves: Advancing the optical phase of one plane wave by one radian correspondingly advances the spatial phase of the fringe pattern by one radian. Since the intensity of the interference pattern at any location is maximal if and only if the phases of the two plane waves are equal at that location, the phases can be aligned by probing the intensity at that location (e.g., by measuring the light scattered or fluoresced by a small particle placed at that location) and continuously shifting the phase of one of the plane waves until the detected intensity is maximized.

An iterative phase alignment algorithm with an *arbitrary* number of plane waves can be described as follows:

1. Shift the phase of one plane wave until the detected intensity is maximized. This is defined as the first iteration.

2. In the next iteration, shift the phase of a different plane wave wave until the detected intensity is maximized.

3. Repeat the process until the phase of every plane wave has been adjusted once. This is defined as one set of iterations.

With a large number of plane waves, the behavior of the iterative phase alignment algorithm is not transparent. For example, the phases of the plane waves are in general not perfectly equal after one set of iterations. However, analysis leads to a simple and intuitive geometric interpretation of the iterative phase alignment algorithm in the complex plane. Subsequently, one can show that the iterative algorithm is guaranteed to converge monotonically using a geometric argument.

4.2.1 Geometric Interpretation in the Complex Plane

The standing wave generated by N electromagnetic plane waves of identical temporal frequency can be written

$$\mathbf{E}(\mathbf{r}) = \sum_{n=1}^{N} \mathbf{E}_n \exp(j\mathbf{k}_n \cdot \mathbf{r}), \tag{4.1}$$

where $\mathbf{E}_n$ and $\mathbf{k}_n$ denote the complex electric-field vector and wave vector of the nth plane wave, respectively, and $\mathbf{r}$ is a 3-D position vector (i.e., $\mathbf{r} = \hat{\mathbf{x}}x + \hat{\mathbf{y}}y + \hat{\mathbf{z}}z$). The interference pattern $I(\mathbf{r})$, which we assume to be proportional to time-averaged electric energy density, can be related to the standing wave by

$$\begin{aligned} I(\mathbf{r}) &= \left\langle \|\mathbf{E}(\mathbf{r},t)\|^2 \right\rangle && (4.2)\\ &= \frac{1}{2}\Re\left\{\mathbf{E}(\mathbf{r}) \cdot \mathbf{E}^*(\mathbf{r})\right\} && (4.3)\\ &= \sum_{n=1}^{N} \frac{\|\mathbf{E}_n\|^2}{2} + \sum_{m=1}^{N-1}\sum_{n=m+1}^{N} |\mathbf{E}_m| \cdot |\mathbf{E}_n| \cos[(\mathbf{k}_m - \mathbf{k}_n)\cdot\mathbf{r} + (\phi_m - \phi_n)], && (4.4) \end{aligned}$$

where $\langle\cdot\rangle$ denotes time-averaging, $\|\cdot\|$ denotes length, $\Re\{\cdot\}$ denotes "the real part of," * denotes complex conjugate, $|\cdot|$ denotes magnitude (i.e., complex modulus), and ϕ_n is the phase of the nth plane wave. Assuming for simplicity that $\mathbf{E}_m = \mathbf{E}_n$ for all

m and n (i.e., the amplitudes of all the plane waves are equal and the polarization vectors of all the plane waves are equal), Eq. 4.4 can be rewritten

$$I(\mathbf{r}) = A + B \sum_{m=1}^{N-1} \sum_{n=m+1}^{N} \cos[(\mathbf{k}_m - \mathbf{k}_n) \cdot \mathbf{r} + (\phi_m - \phi_n)], \tag{4.5}$$

where A and B are real constants.

Let us now consider one iteration of the phase alignment algorithm. With no loss of generality, we may define the plane-wave phase which is adjusted as ϕ_1 and assume that the location of phase alignment is the origin (i.e., $\mathbf{r} = 0$). Consequently, the detected intensity can be written as a function of ϕ_1 alone:

$$\begin{aligned}
I_1(\phi_1) &= I(\mathbf{r})|_{\mathbf{r}=0} && (4.6)\\
&= A + B \sum_{m=1}^{N-1} \sum_{n=m+1}^{N} \cos(\phi_m - \phi_n) && (4.7)\\
&= C + B \sum_{m=2}^{N} \cos(\phi_1 - \phi_m) && (4.8)\\
&= C + \frac{B}{2} \left[\exp(j\phi_1) \sum_{m=2}^{N} \exp(-j\phi_m) + \exp(-j\phi_1) \sum_{m=2}^{N} \exp(j\phi_m) \right], && (4.9)
\end{aligned}$$

where C is a real constant. If we define

$$\Phi \equiv \angle \left\{ \sum_{m=2}^{N} \exp(j\phi_m) \right\}, \tag{4.10}$$

where $\angle\{\cdot\}$ denotes "the angle of," Eq. 4.9 simplifies to

$$I_1(\phi_1) = C + D \cos(\phi_1 - \Phi), \tag{4.11}$$

where D is a real constant. From Eq. 4.11 we see that the detected intensity $I_1(\phi_1)$ is maximal when $\phi_1 = \Phi$. Thus, one iteration of the phase alignment algorithm is equivalent to setting the phase of one plane wave ϕ_1 to the angle Φ defined in Eq. 4.10. This process is readily visualized in the complex plane.

Fig. 2 illustrates a geometric interpretation of one iteration of the phase alignment

algorithm in the complex plane. The phase of each plane wave ϕ_m can be represented by the complex phase vector $\exp(j\phi_m)$. The complex phase vectors of ten plane waves before and after one iteration of the algorithm are shown. The arrow in the right panel indicates the sum vector $\sum_{m=2}^{N} \exp(j\phi_m)$ which defines Φ in Eq. 4.10.

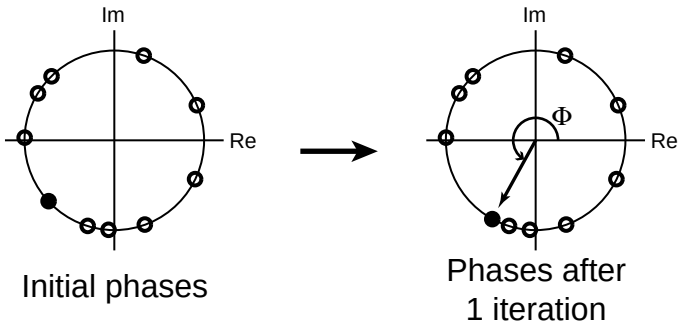

Figure 4-2: Geometric interpretation in the complex plane. The large circle in each panel indicates the unit circle in the complex plane. Each small circle indicates a complex phase vector which represents the phase of a plane wave. The left panel shows the phases of ten plane waves, which are initially randomly distributed. The right panel shows the phases of the ten plane waves after one iteration of the phase alignment algorithm. One iteration can be interpreted geometrically as setting the phase of one plane wave (solid circle) to Φ, the angle defined by the sum of the other nine complex phase vectors (arrow).

4.2.2 Monotonic Convergence

Fig. 3 shows the complex phase vectors of ten plane waves after 10, 20, and 30 iterations of the phase alignment algorithm. The gray arrow in each panel indicates the arithmetic mean vector $\boldsymbol{\mu}$ of the complex phase vectors:

$$\boldsymbol{\mu} = \frac{1}{N} \sum_{m=1}^{N} \exp(j\phi_m). \tag{4.12}$$

Note that the magnitude of $\boldsymbol{\mu}$ is initially much smaller than unity. As the plane-wave phases approach alignment, the magnitude of $\boldsymbol{\mu}$ approaches unity. Therefore, the convergence properties of the iterative phase alignment algorithm can be studied by examining the evolution of $|\boldsymbol{\mu}|$.

After one iteration, the new arithmetic mean vector $\boldsymbol{\mu\prime}$ is

$$\boldsymbol{\mu\prime} = \frac{1}{N} \left[\exp(j\Phi) + \sum_{m=2}^{N} \exp(j\phi_m) \right], \tag{4.13}$$

where Φ is defined in Eq. 4.10. If we can show that $|\boldsymbol{\mu\prime}| \geq |\boldsymbol{\mu}|$, then the phase

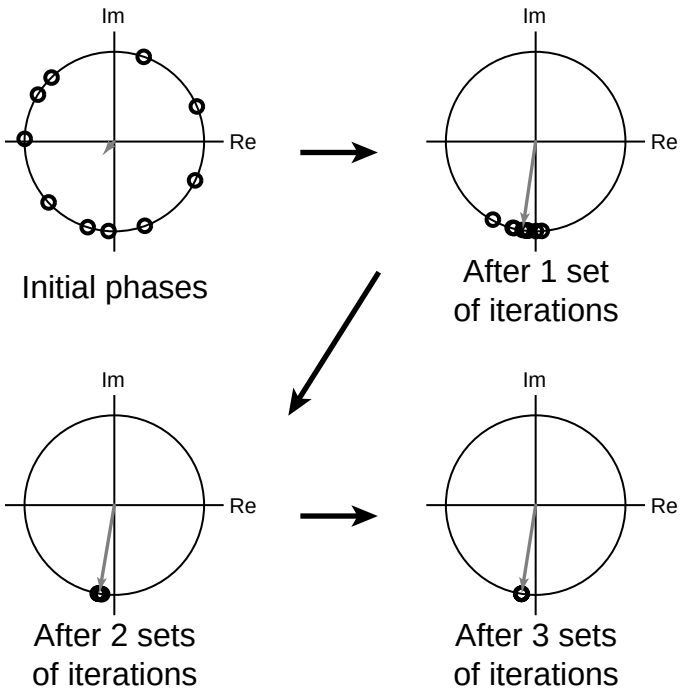

Figure 4-3: Phase alignment after multiple sets of iterations. Note that phase alignment improves after each set of iterations. The gray arrow in each panel indicates the arithmetic mean vector $\boldsymbol{\mu}$.

alignment algorithm converges monotonically. With this in mind, we write

$$
\begin{aligned}
|\boldsymbol{\mu\prime}|^2 - |\boldsymbol{\mu}|^2 &= \boldsymbol{\mu\prime}\boldsymbol{\mu\prime}^* - \boldsymbol{\mu}\boldsymbol{\mu}^* && (4.14)\\
&= \frac{1}{N^2}\left\{\sum_{m=2}^{N} \exp[j(\Phi - \phi_m)] + \exp[-j(\Phi - \phi_m)]\right. \\
&\qquad \left. - \sum_{m=2}^{N} \exp[j(\phi_1 - \phi_m)] + \exp[-j(\phi_1 - \phi_m)]\right\} && (4.15)\\
&= \frac{1}{N^2}\left\{[\exp(j\Phi) - \exp(j\phi_1)] \sum_{m=2}^{N} \exp(-j\phi_m)\right. \\
&\qquad \left. + [\exp(-j\Phi) - \exp(-j\phi_1)] \sum_{m=2}^{N} \exp(j\phi_m)\right\}. && (4.16)
\end{aligned}
$$

The geometric interpretation in the complex plane tells us

$$
\exp(j\Phi) = \frac{\sum_{m=2}^{N} \exp(j\phi_m)}{\left|\sum_{m=2}^{N} \exp(j\phi_m)\right|}. \tag{4.17}
$$

Substituting into Eq. 4.16,

$$
\begin{aligned}
|\boldsymbol{\mu\prime}|^2 - |\boldsymbol{\mu}|^2 &= \frac{1}{N^2}\left\{\left|\sum_{m=2}^{N} \exp(j\phi_m)\right| - \exp(j\phi_1) \sum_{m=2}^{N} \exp(-j\phi_m)\right. \\
&\qquad \left. + \left|\sum_{m=2}^{N} \exp(j\phi_m)\right| - \exp(-j\phi_1) \sum_{m=2}^{N} \exp(j\phi_m)\right\}. && (4.18)
\end{aligned}
$$

Recognizing the two complex terms in Eq. 4.18 as complex conjugates, since $\mathbf{ab} + (\mathbf{ab})^* = |\mathbf{a} + \mathbf{b}^*|^2 - (\mathbf{aa}^* + \mathbf{bb}^*)$, Eq. 4.18 can be rewritten

$$
\begin{aligned}
|\boldsymbol{\mu\prime}|^2 - |\boldsymbol{\mu}|^2 &= \frac{1}{N^2}\left\{1 + 2\left|\sum_{m=2}^{N} \exp(j\phi_m)\right| + \left|\sum_{m=2}^{N} \exp(j\phi_m)\right|^2\right. \\
&\qquad \left. - \left|\sum_{m=1}^{N} \exp(j\phi_m)\right|^2\right\} && (4.19)\\
&= \frac{1}{N^2}\left\{\left[1 + \left|\sum_{m=2}^{N} \exp(j\phi_m)\right|\right]^2 - \left|\sum_{m=1}^{N} \exp(j\phi_m)\right|^2\right\} && (4.20)
\end{aligned}
$$

Since $|\exp(j\phi_1)| = 1$, we see that the quantity in Eq. 4.20 is always greater than or

equal to zero. Since the magnitude of a complex number is always nonnegative,

$$|\boldsymbol{\mu\prime}| \geq |\boldsymbol{\mu}|. \tag{4.21}$$

Thus, the iterative algorithm is guaranteed to converge monotonically. The only case in which $|\boldsymbol{\mu\prime}| = |\boldsymbol{\mu}|$ corresponds to $\Phi = \phi_1$, which is the trivial case in which ϕ_1 is unchanged between iterations.

4.3 Numerical Experiments

Root-mean-square (RMS) phase alignment error $E(\phi_1..\phi_N)$ can be defined simply as

$$E(\phi_1..\phi_N) = \sqrt{\frac{1}{N}\sum_{m=2}^{N}(\phi_m - \phi_1)^2}, \tag{4.22}$$

where the value of $(\phi_m - \phi_1)$ is between $-\pi$ and π. If all the plane-wave phases are equal, $E(\phi_1..\phi_N) = 0$.

Fig. 4 shows mean RMS phase alignment error on a logarithmic vertical scale for 1,000 numerically simulated phase alignments. Before phase alignment, mean error is between 1.47 and 1.71 radians for 10 and 100 plane waves, respectively. After one set of iterations (i.e., N iterations), mean error is .105 and .0559 radians with 10 and 100 plane waves, respectively. After the first set of iterations, the logarithm of mean RMS phase alignment error as a function of iterations decreases approximately linearly with a slope of $-2.3/N$.

Since the detected intensity during each iteration of phase alignment is sinusoidal, the amount of modulation in detected intensity can be quantified using the common measure of fringe visibility. Fringe visibility $\mathcal{V}(\phi_1..\phi_N)$ during each iteration can be defined starting from Eq. 11 as

$$\mathcal{V}(\phi_1..\phi_N) = \frac{\max\{I_1(\phi_1)\} - \min\{I_1(\phi_1)\}}{\max\{I_1(\phi_1)\} + \min\{I_1(\phi_1)\}} \tag{4.23}$$

$$= \frac{(C+D) - (C-D)}{(C+D) + (C-D)} \tag{4.24}$$

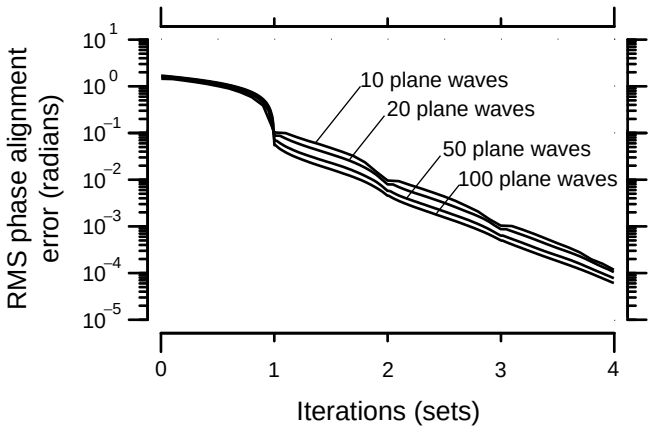

Figure 4-4: Phase alignment error as a function of number of iterations. The plot shows the mean RMS phase alignment error of 1,000 simulated phase alignments with 10, 20, 50, and 100 plane waves. Plane-wave phases were randomly distributed at the start of each phase alignment.

$$= \frac{\left|\sum_{m=2}^{N} \exp(j\phi_m)\right|}{N/2 + \sum_{m=1}^{N-1}\sum_{n=2}^{N} \cos(\phi_m - \phi_n)}. \tag{4.25}$$

Note that our "visibility" quantifies modulation in measured intensity as a function of time, rather than as a function of space.

Fig. 5 shows mean fringe visibility on a logarithmic vertical scale for 1,000 numerically simulated phase alignments. During the first iteration, mean fringe visibility is 0.69, 0.55, 0.40, and 0.29 with 10, 20, 50, and 100 plane waves, respectively. After the first set of iterations (i.e., N iterations), mean fringe visibility is nearly constant at approximately $2.1/N$. Mean fringe visibility is highest with the fewest number of plane waves.

4.4 Experimental Verification

Fig. 6 shows the measured PSF of a scanning SWI microscope before and after one phase alignment. The PSF was measured by imaging an isolated 100-nm-diameter polystyrene microsphere (Molecular Probes, Inc., Eugene, Oregon). The microsphere sample was prepared by drying a 1.0 μl drop of microsphere solution (1000:1 dilution in water) in air on a no.-1-thickness cover glass. Microspheres were imaged in air

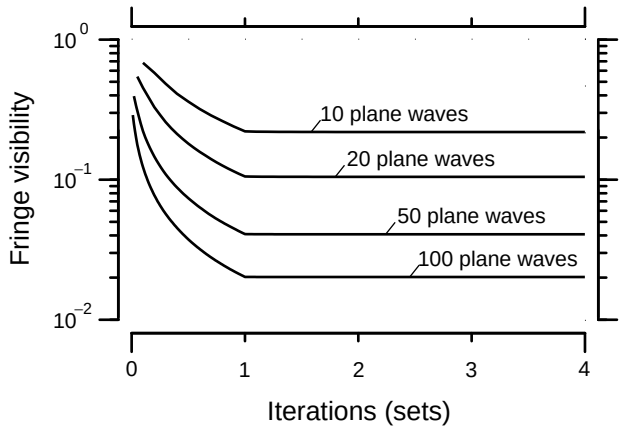

Figure 4-5: Effects of number of plane waves on fringe visibility. The plot shows the mean fringe visibility of 1,000 simulated phase alignments with 10, 20, 50, and 100 plane waves. Plane-wave phases were randomly distributed at the start of each phase alignment.

on top of the cover glass (i.e., microspheres were illuminated directly and imaged through the cover glass).

The scanning SWI microscope features illumination generated by the interference of 15 linearly-polarized laser beams ($\lambda = 488$ nm) split from a 700-mW single-frequency argon ion laser (Coherent, Inc., Santa Clara, California). The 15 beams are directed by an assembly or mirrors into a converging circular cone with a half-angle of 72 degrees, corresponding to a NA of 0.95. One mirror in each beam path is mounted on a piezoelectric actuator, allowing the phase of each beam to be modulated independently. The beams are TM-polarized with respect to the image plane, resulting in radially-polarized illumination. The SWI apparatus is described in more detail elsewhere.

The microsphere sample is mounted on a two-axis closed-loop piezoelectric scanning stage (Melles Griot, Carlsbad, California). As the sample is scanned through the SWI pattern, light scattered by the microsphere is collected by an $10\times$ / 0.20 NA objective lens and focused onto a 15-μm-diameter pinhole at the image plane. Behind the pinhole, scattered light is measured by a photon-counting photomultiplier tube (Hamamatsu Photonics, Bridgewater, New Jersey). The pixels spacing is 50 nm, and the pixel dwell time is 50 ms.

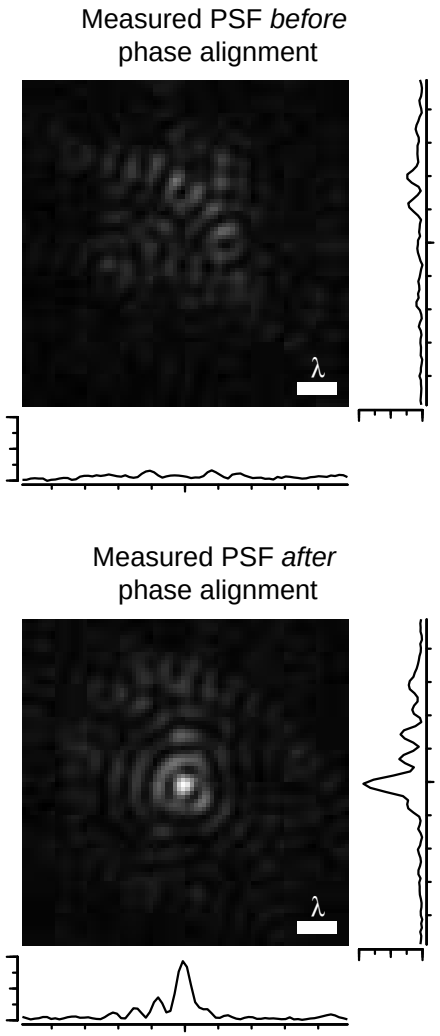

Figure 4-6: Experimentally measured PSFs before and after phase alignment. The two panels show the measured lateral responses of a scanning SWI microscope to a 100-nm-diameter microsphere. The top panel shows the response before phase alignment. The bottom panel shows the response after 15 iterations (one set) of the phase alignment algorithm. The intensities of the center row and column of pixels are plotted below and to the right of each image, respectively.

One iteration of the phase alignment algorithm is implemented experimentally by shifting the phase of one laser beam through one cycle at approximately eighth-wavelength steps (i.e., $2\pi/8$-radian steps). The intensity of light scattered by the microsphere at each eighth-wavelength step is measured with the photomultiplier tube (PMT). The eight intensity values are then least-squares fit to an offset sinusoid to determine the phase shift which maximizes the intensity of light scattered by the microsphere. The phase of the laser beam is then shifted appropriately. The PMT integration time at each step is 20 ms. One set of iterations (i.e., 15 iterations) is completed in 37 s. Approximately 94% of the 37 s is used for drift and hysteresis compensation for the open-loop piezoelectric actuators which shift the phases of the laser beams.

Before phase alignment, the measured lateral response to a 100-nm-diameter microsphere (Fig. 6, top) reveals that the laser-beam phases are essentially random. After one set of phase-alignment iterations, the measured response (Fig. 6, bottom) reveals constructive interference at the location where phase alignment occurred. The full-width at half-maximum intensity diameter of the measured response is approximately 220 nm.

4.5 Discussion

One set of iterations is likely adequate for imaging in scanning SWI microscopy, regardless of the number of planar wavefronts. In theory, the mean RMS phase alignment error is on the order of 0.1 radians after one set of iterations, and the intelligibility of images is not significantly degraded with random phase errors in spatial frequency on the order of 0.1 radians. However, for quantitative analysis of images obtained with scanning SWI microscopy (e.g., deconvolution with a theoretical PSF), multiple sets of iterations may be required.

The issue of whether the phase alignment technique is suitable for use with more than a hundred planar wavefronts is addressed in the numerical simulations. Specifically, phase alignment error after one set of iterations is actually *smaller* with a

larger number of wavefronts. One intuitive explanation is that the arithmetic mean vector possesses more "inertia" with a larger number of wavefronts, resulting in more accurate phase alignment. Unfortunately, fringe visibility is also smaller with a larger number of wavefronts. Low fringe visibility may limit the maximum number of wavefronts that can be aligned using the iterative phase alignment algorithm. However, the problem may be solved with slight modifications to the algorithm.

For example, 10,000 wavefronts can be aligned in 100 groups of 100 wavefronts. During each iteration, if the 9,900 wavefronts not involved in alignment are blocked, fringe visibility is determined by only 100 wavefronts. Inter-group phase alignment requires 10,000 iterations. Intra-group phase alignment can be accomplished in 100 subsequent iterations. Measured in iterations, the overhead for the modified algorithm is only 1%. However, note that 99% of the beams are blocked (i.e., do not illuminate the sample) during phase alignment. In situations where the speed of phase alignment is light-limited, the modified algorithm is slower by more than a factor of 100. Also, note that the modified algorithm requires additional optical apparatus. One of the strengths of the unmodified iterative phase alignment algorithm is that it does not require optical apparatus beyond what is already contained in a scanning SWI microscope.

The iterative phase alignment algorithm was developed with simplicity of analysis and implementation in mind. Alternate techniques may exist which converge more quickly. For example, simultaneous adjustment of multiple plane-waves phases may be desirable. Also, a small point-like particle is not the only suitable phase-alignment sample. In theory, any well-characterized sample with sufficiently high spatial-frequency content may be used for phase alignment. A principal advantage of using a more complex sample is that it would scatter (or fluoresce) more light, resulting in faster and more accurate phase alignment.

4.6 Conclusion

Phase alignment of is a new problem in microscopy necessitated by the advent of SWI microscopes with large numbers of wavefronts. We have described, analyzed, and demonstrated experimentally a simple technique for phase alignment with large number of wavefronts. The technique is currently in use in the first scanning SWI fluorescence microscope, and we expect that the technique will be of great utility to SWI microscopy.

Chapter 5

High-resolution microscopy without high-numerical-aperture lenses: scanning standing-wave illumination fluorescence microscopy

Abstract

We propose and demonstrate a new type of far-field fluorescence microscope capable of sub-λ resolution without high numerical aperture (NA) optical components. In the new scanning standing-wave illumination fluorescence microscope, focused illumination is generated by the interference of a large number of planar wavefronts. The technical complexities of controlling the large number of wavefront phases are overcome with scanning and confocal detection. A measured point spread function less than 290 nm in lateral diameter ($\lambda_{\text{exc}} = 488$ nm) is achieved using fifteen planar illumination wavefronts and a 0.25-NA objective lens.

The concept of resolution improvement in far-field fluorescence microscopy using the

interference of coherent planar wavefronts has been proposed and demonstrated in numerous configurations [7, 8, 9, 11, 12, 13, 14, 15, 16, 17, 19]. In the recently proposed scanning standing-wave illumination (SWI) fluorescence microscope, it has been demonstrated theoretically that with a sufficiently large number of planar wavefronts, SWI can be the *primary source* of resolution rather than a secondary means for resolution enhancement. In theory, sub-wavelength resolution can be achieved using only low numerical aperture (NA) optics. Because the SWI pattern can be stationary in the scanning mode of image formation, the complexity of controlling a large number of planar wavefronts is reduced. Consequently, it has been possible to construct a prototype scanning SWI fluorescence microscope which successfully controls 15 laser beams. In the manuscript, we report the first imaging results obtained with scanning SWI fluorescence microscopy.

The prototype microscope is shown in in Fig. 1. The microscope can be described as a Type 2 scanning fluorescence microscope where the illumination objective lens has been replaced by SWI [36]. A stationary SWI pattern is generated by the interference of 15 linearly-polarized laser beams (λ = 488 nm) split from a 700-mW single-frequency argon ion laser (Coherent, Inc., Santa Clara, California). The 15 beams are directed by an assembly or mirrors into a converging circular cone with a half-angle of 72 degrees, corresponding to a NA of 0.95. One mirror in each beam path is mounted on a piezoelectric actuator, allowing the phase of each beam to be modulated independently. The beams are TM-polarized with respect to the image plane, resulting in radially-polarized illumination. The SWI apparatus is described in more detail elsewhere. The sample is mounted on a two-axis closed-loop piezoelectric scanning stage (Melles Griot, Carlsbad, California). As the sample is scanned, light fluoresced by the sample is collected by an 10 $\times$ / 0.25 NA objective lens and focused onto a 15-μm-diameter pinhole at the image plane. Excitation light is rejected by a 3-mm-thick OG-515 color glass filter (Schott, Inc., Elmsford, New York), and fluoresced light is measured by a photon-counting photomultiplier tube (Hamamatsu Photonics, Bridgewater, New Jersey).

The relative phases of the 15 lasers beams are initially random because the SWI

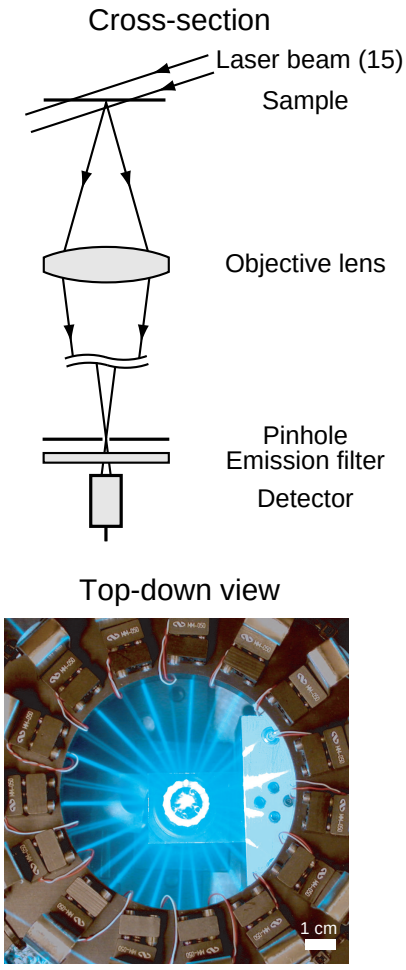

Figure 5-1: Scanning standing-wave illumination fluorescence microscope with 15 laser beams. See text for details.

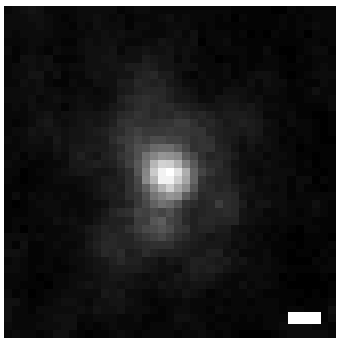

Figure 5-2: Measured two-dimensional lateral response to a 200-nm-diameter fluorescent microsphere. The pixel spacing is 50 nm, and the FWHM diameter is approximately 290 nm. The center row of pixels is plotted in Fig. 3. The scale bar denotes 200 nm.

apparatus contains macroscopically-positioned optical components. The phases of the 15 beams are aligned by placing an isolated 200- or 500-nm-diameter fluorescent microsphere (Molecular Probes, Inc., Eugene, Oregon) at the center of the field of view and then iteratively adjusting the phase of each beam to maximize the intensity of light fluoresced by the microsphere. In the absence of noise, this algorithm is guaranteed to converge monotonically and results in a mean RMS phase alignment error of 0.1 radians after the phase of each beam is adjusted once.

Fig. 2 shows the measured two-dimensional lateral response of the microscope to an isolated 200-nm-diameter fluorescent microsphere. The microsphere sample was prepared by drying a 1.0 μl drop of microsphere solution (1000:1 dilution in water) in air on a no.-1-thickness cover glass. Microspheres were imaged in air on top of the cover glass (i.e., microspheres were illuminated directly and imaged through the cover glass). The phases of the 15 laser beams were aligned at a nearby microsphere (not shown) less than one minute prior to imaging. The pixel dwell time was 50 ms.

The theoretical PSF $h(\mathbf{r})$ of a scanning SWI fluorescence microscope can be expressed as the product of the SWI pattern and the PSF of the objective lens $h_1(\mathbf{r})$:

$$h(\mathbf{r}) = \left\{ \sum_{n=1}^{N} \frac{\|\mathbf{E}_n\|^2}{2} + \sum_{m=1}^{N-1} \sum_{n=m+1}^{N} |\mathbf{E}_m| \cdot |\mathbf{E}_n| \cos[(\mathbf{k}_m - \mathbf{k}_n) \cdot \mathbf{r} + (\phi_m - \phi_n)] \right\} h_1(-\mathbf{r}), \tag{5.1}$$

where $\mathbf{r}$ is a 3-D position vector (i.e., $\mathbf{r} = \hat{\mathbf{x}}x + \hat{\mathbf{y}}y + \hat{\mathbf{z}}z$), N is the number of SWI plane waves, $\|\cdot\|$ denotes length, $\mathbf{E}_n$ is the complex electric-field vector and wave vector of the nth plane wave, $|\cdot|$ denotes magnitude (i.e., complex modulus), $\mathbf{k}_n$ and ϕ_n are the wave vector and phase of the nth plane wave, respectively, and $h_1(\mathbf{r})$ is the incoherent PSF of the objective lens. The FWHM diameter of the theoretical PSF of the prototype microscope is 190 nm. The theoretical optical transfer function (OTF) of the prototype microscope is contiguous and generally strong throughout the passband, which extends in spatial frequency up to 1/210 nm^{-1}.

The continuous solid curve in Fig. 3 shows the theoretical lateral response of the prototype microscope calculated by convolving the theoretical PSF with a 200-nm-diameter sphere. The amplitudes and wavelengths of all the SWI plane waves were equal, and phases were equal at the center of the PSF. The PSF of the objective lens $h_1(\mathbf{r})$ was calculated by convolving a 15 μm/10×-diameter circular flat-top function (the pinhole) with the PSF of a diffraction-limited incoherent imaging system with a circular pupil function:

$$h_1(\mathbf{r}) = \left[\frac{J_1(2\pi w r)}{\pi w r}\right]^2, \tag{5.2}$$

where $r = \|\mathbf{r}\|$, J_1 is the first-order Bessel function of the first kind, and $w = \text{NA}/\lambda_{em} = 0.25/540$ nm [37]. The wavelength of the fluoresced light λ_{em} was estimated as the centroid of the product of the fluorescence emission spectrum and the filter transmittance spectrum.

The piecewise linear curve in Fig. 3 shows the measured lateral response of the prototype microscope. The FWHM diameter of measured response is 38% wider than the theoretical response. The principal reasons for widening are believed to be unequal beam amplitudes and errors in phase alignment. Additionally, the reflection of the beams off the cover glass was not accounted for in the theoretical response; incorporating the reflection of the beams (i.e., introducing a second set of beam waves with a reflection coefficient $\Gamma = -0.24$) widens FWHM diameter of the PSF at the air-to-glass interface by approximately 5%.

For comparison, the dashed curve in Fig. 3 shows the theoretical lateral response

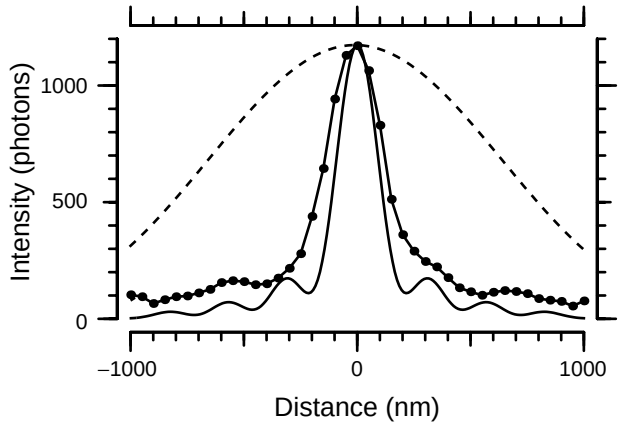

Figure 5-3: Comparison of one-dimensional lateral responses to a 200-nm-diameter fluorescent microsphere. The plot shows the theoretical (continuous solid) and measured (piecewise-linear) lateral responses with SWI and the theoretical lateral response with conventional uniform illumination (dashed). The FWHM diameters are 210 nm, 290 nm, and 1500 nm, respectively.

of the objective lens with conventional uniform illumination. The FWHM diameter of the theoretical and measured lateral responses with SWI are 7.1 and 5.2 times narrower, respectively, than with conventional resolution. By classical resolution criteria (e.g., the Houston criterion [66]), resolution has been increased by a factor of 7.1 or 5.2. However, because the shapes of the SWI OTF and conventional-illumination OTF are dissimilar, *detected* resolution is more appropriate for comparison than calculated resolution [67].

Fig. 4 shows the response of the microscope to a cluster of 500-nm-diameter fluorescent microspheres. The 500-nm-diameter microsphere sample was prepared and imaged using the same protocols as for the 200-nm-diameter microsphere sample. The pixel dwell time for the SWI image was 50 ms. While the illumination intensity for the conventional-illumination image was a factor of 15 lower, the pixel dwell time was a factor of 30 higher. Intentionally doubling the number of photons detected in the conventional-illumination image ensured that the SWI image did not have a signal-to-noise advantage before subsequent image processing.

Fig. 5 shows images generated from those in Fig. 4 after 2-D linear filtering by

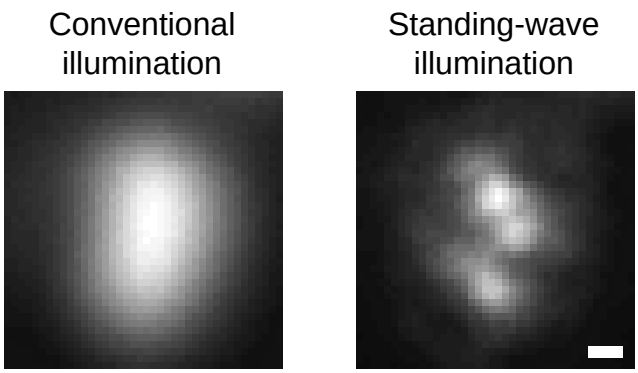

Figure 5-4: Comparison of unprocessed images of a cluster of 500-nm-diameter fluorescent microspheres. The two panels show measured images of the identical region taken with the same objective lens. The conventional-illumination image was generated by blocking all but one of the 15 SWI beams and increasing the exposure time by a factor of 30. The scale bar denotes 500 nm.

the approximate inverse of of each OTF:

$$H^{-1}(\mathbf{f}) \approx \frac{H^*(\mathbf{f})}{|H(\mathbf{f})|^2 + \mu}, \tag{5.3}$$

where $H(\mathbf{f})$ is the OTF, where $\mathbf{f}$ is a spatial-frequency vector, * denotes complex conjugate, and μ is a regularization parameter [43]. The OTF was estimated as the Fourier transform of the 2-D lateral response to a nearby isolated 500-nm-diameter fluorescent microsphere (not shown). Again, intentionally doubling the number of photons detected in the conventional-illumination PSF measurement ensured that the SWI PSF was not known with better accuracy. The maximum filter gain was set identically to 10.0 for both images by normalizing $H(\mathbf{f})$ and setting μ to 0.025. The sample was known to be composed of 500-nm-diameter microspheres. The SWI image (Fig. 5, right) is consistent with this fact. In the conventional-illumination image (Fig. 5, left), it is difficult to conclude that the sample is composed of microspheres. Increasing the filter gain beyond 10.0 (not shown) for the conventional-illumination image fails to resolve the two upper microspheres, or even to indicate the orientation between the two microspheres.

Resolution in scanning SWI fluorescence microscopy is governed by the familiar

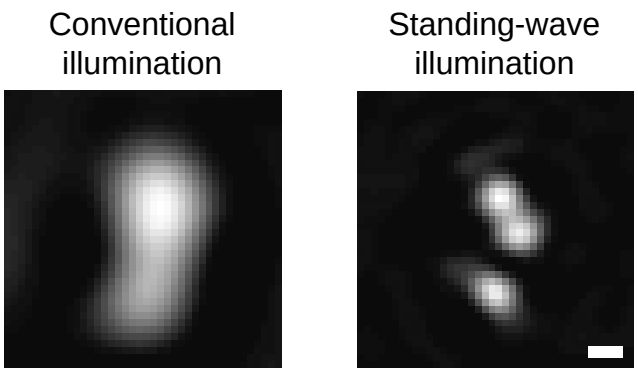

Figure 5-5: Comparison of processed images of a cluster of 500-nm-diameter fluorescent microspheres. The two panels show images generated from those in Fig. 4 after linear inverse filtering. The maximum filter gain was set identically to 10.0 for both images. The scale bar denotes 500 nm.

diffraction limit and consequently will not exceed the resolution of 4Pi-confocal fluorescence microscopy [65]. In fact, fluorescence microscopy with SWI may be poorly suited for several applications. For example, the "haze" surround the microspheres in the unprocessed SWI image (Fig. 4, right) is caused by a "spike" at zero spatial frequency in the OTF. This spike is inherent to all SWI fluorescence microscopes and "wastes" photons on redundant low-frequency information compared to conventional fluorescence microscopy techniques. Also, although high-NA SWI increases the maximum measured spatial frequency, it does not increase the amount of light collected by the microscope as a high-NA imaging objective lens would.

The value of SWI microscopy with large numbers of planar wavefronts may lie in its lensless approach to high-resolution microscopy. For example, the SWI apparatus has a NA of 0.95 NA and working distance of 22 mm; it produces diffraction-limited illumination with a front aperture over 140 mm in diameter, a feat not easily achieved with lens-based optics. Also, since the optical path of the SWI apparatus consists entirely of flat mirrors (with the exception of a beam expander), the technique may scale to x-ray wavelengths.

In theory, high-NA SWI can be the primary source of resolution in a microscope, enabling high-resolution microscopy using only low-NA optics. To that end, we have constructed a prototype scanning SWI fluorescence microscope with 15 laser beams.

We have experimentally characterized the PSF of the microscope by measuring the lateral response and demonstrated an improvement in resolution over conventional uniform illumination by imaging a cluster of microspheres.

Chapter 6

Conclusion

The long-term goal of this work is to scale scanning SWI microscopy to x-ray wavelengths, possibly for biological imaging at soft x-ray wavelengths with nanometer resolution. The technologies required for implementing the SWI apparatus at x-ray wavelengths can be grouped into five categories: (1) coherent x-ray sources, (2) mirrors, (3) phase modulators, (4) low-NA objective lenses, and (5) detectors. All five categories can be addressed with existing or near-future technologies.

Many of the synchrotron-based x-ray sources used in current x-ray microscopes produce x-ray beams with sufficient temporal and spatial coherence for scanning SWI microscopy [68, 69, 70, 71, 56, 72]. "Table-top" sources of coherent x-rays (i.e., sources that fit on a laboratory optical table) are an active area of research [48, 73, 74]. Promising table-top coherent x-ray sources under development include high harmonic generation [75, 76, 51, 77] and soft x-ray lasers [78, 79, 48, 49]. Additionally, x-ray free-electron lasers are expected to be available within a decade and should generate coherent x-ray beams of unprecedented brightness [50, 52, 80].

Mirrors, phase modulators, low-NA objective lenses, and detectors suitable for use in scanning SWI x-ray microscopy are currently available. Efficient normal-incidence mirrors can be constructed with multilayer structures [81, 82]. Alternatively, the SWI apparatus can be designed with grazing-incidence reflections alone, in which case single-surface mirrors would suffice [83]. Phase modulation can be achieved using commercially available closed-loop piezoelectric actuators with subnanometer

resolution (e.g., Mad City Labs or Polytec PI), or potentially with more precision using reflective acousto-optic phase modulators [84, 85]. Zone-plate objectives have been developed extensively for use at x-ray wavelengths and are used currently in x-ray microscopes [22, 83]. X-ray detectors and imagers are commercially available (e.g., Hamamatsu or Amptek).

Besides implementation of the SWI apparatus at x-ray wavelengths, the premise of x-ray microscopy with nanometer resolution assumes the resolution of at least two additional issues: specimen damage and speckle. Specimen damage fundamentally limits the maximum resolution of *any* imaging technique. The principal contrast mechanism in water-window x-ray microscopy is absorption (as opposed to scattering, which is the principal contrast mechanism in x-ray crystallography and electron microscopy). Since contrast depends intrinsically on the absorption of ionizing radiation, resolution comes at the cost of breakage of chemical bonds. Theoretical estimates of maximum resolution for biological specimens conflict. A comprehensive review article on soft x-ray microscopy stated in 1995 that maximum resolution would be approximately 10 nm in frozen biological specimens [21]. A different review article on radiation damage stated in 1995 maximum resolution would be approximately 50 nm [86]. Experimental reports of resolution include 35 nm in 1998 [87] and better than 50 nm with "virtually no detectable change in ultrastructure ... after 40 consecutive images" in 2000 [88].

While the ultimate resolution limit in biological specimens is still uncertain, nanometer resolution may very well turn out to be unattainable. Nonetheless, resolution improvement in x-ray microscopy is still a valuable goal. Resolution is not currently limited by specimen damage, so there is certainly significant "room for improvement." Also, damage issues are not as critical in *periodic* samples; scanning SWI microscopy may turn out to be best-suited for tackling the phase problem in x-ray crystallography [89]. It should also be noted that non-biological samples are far more robust to x-ray radiation [46]. Still, resolution in hard x-ray microscopy of non-biological samples is currently limited by fabrication tolerances in the construction of hard x-ray imaging optics (e.g., zone plates, refractive metallic lenses, and

Kirkpatrick-Baez mirrors) to approximately 100 nm [90]. Scanning SWI microscopy could advance x-ray microscopy to the state where resolution is limited only by specimen damage, and not intrinsically by the microscope itself.

The second issue of speckle arises from the imaging of coherent illumination [91, 92]. In the imaging results reported in this thesis, difficulties associated with speckle were circumvented by the use of fluorescence imaging; although the illumination was coherent, the imaged fluoresced light was *incoherent*. Unfortunately, speckle is expected to affect scanning SWI x-ray microscopy images since absorption is the principal contrast mechanism. Speckle appears typically in images as high-frequency multiplicative noise and consequently greatly reduces image intelligibility.

Two factors however may alleviate the effects of speckle in scanning SWI x-ray microscopy. First, the low amount of scattering and the homogeneity of refractive index of materials at x-ray wavelengths may result in substantially less speckle than one would expect from coherent imaging at visible wavelengths. Second, the correlation length or "blob size" of speckle is determined by the NA (i.e., the maximum spatial frequency in the OTF) of the *imaging* optics [92]. One of the unique properties of SWI microscopy with large numbers of wavefronts is that the maximum spatial frequency in the overall OTF can be significantly higher than in the objective-lens OTF: speckle may appear as *low*-frequency multiplicative noise. Low-frequency multiplicative noise does not significantly reduce image intelligibility. Potentially, speckle in scanning SWI x-ray microscopy images can be reduced with cepstral filtering [93] or simply tolerated.

Bibliography

[1] D. W. Pohl and L. Novotny, "Near-field optics: Light for the world of NANO," J. Vac. Sci. Technol. B **12**, 1441–1446 (1994).

[2] J. W. Lichtman and S. E. Fraser, "The neuronal naturalist: Watching neurons in their native habitat," Nature Neuroscience **4**, 1215–1220 (2001).

[3] J. Lippincott-Schwartz and G. H. Patterson, "Development and Use of Fluorescent Protein Markers in Living Cells," Science **300**, 87–91 (2003).

[4] E. W.-G. Diau, J. L. Herek, Z. H. Kim, and A. H. Zewail, "Femtosecond Activation of Reactions and the Concept of Nonergodic Molecules," Science **279**, 847–851 (1998).

[5] M. H. Anderson, J. R. Ensher, M. R. Matthews, C. E. Wieman, and E. A. Cornell, "Observation of Bose-Einstein Condensate in a Dilute Atomic Vapor," Science **269**, 198 (1995).

[6] K. B. Davis, M.-O. Mewes, M. R. Andrews, N. J. van Druten, D. S. Durfee, D. M. Kurn, and W. Ketterle, "Bose-Einstein condensation in a gas of sodium atoms," Phys. Rev. Lett. **75**, 3969 (1995).

[7] B. Bailey, D. L. Farkas, D. L. Taylor, and F. Lanni, "Enhancement of axial resolution in fluorescence microscopy by standing-wave excitation," Nature **366**, 44–48 (1993).

[8] M. A. A. Neil, R. Juškaitis, and T. Wilson, "Method of obtaining optical sectioning by using structured light in a conventional microscope," Opt. Lett. **22**, 1905–1907 (1997).

[9] R. Heintzmann and C. Cremer, "Laterally modulated excitation microscopy: improvement of resolution using a diffraction grating," Proc. SPIE **3568**, 185–195 (1998).

[10] M. G. L. Gustafsson, "Extended resolution fluorescence microscopy," Curr. Opin. Struct. Biol. **9**, 627–634 (1999).

[11] M. S. Mermelstein, "Synthetic aperture microscopy," Ph.D. dissertation (Massachusetts Institute of Technology, Cambridge, Mass., 1999).

[12] G. E. Cragg and P. T. C. So, "Lateral resolution enhancement with standing evanescent waves," Opt. Lett. **25**, 46–48 (2000).

[13] M. G. L. Gustafsson, "Surpassing the lateral resolution limit by a factor of two using structured illumination microscopy," Journal of Microscopy **198**, 82–87 (2000).

[14] J. T. Frohn, H. F. Knapp, and A. Stemmer, "True optical resolution beyond the Rayleight limit achieved by standing wave illumination," PNAS **97**, 7232–7236 (2000).

[15] J. T. Frohn, H. F. Knapp, and A. Stemmer, "Three-dimensional resolution enhancement in fluorescence microscopy by harmonic excitation," Opt. Lett. **26**, 828–830 (2001).

[16] P. T. C. So, H.-S. Kwon, and C. Y. Dong, "Resolution enhancement in standing-wave total internal reflection microscopy: a point-spread engineering approach," J. Opt. Soc. Am. A **18**, 2833–2845 (2001).

[17] R. Heintzmann, T. M. Jovin, and C. Cremer, "Saturated patterned excitation microscopy—a concept for optical resolution improvement," J. Opt. Soc. Am. A **19**, 1599–1609 (2002).

[18] J. Ryu, B. K. P. Horn, M. S. Mermelstein, S. S. Hong, and D. M. Freeman, "Application of structured illumination in nano-scale vision," presented at the IEEE Workshop on Computer Vision for the Nano-Scale, Madison, Wisconsin, 16–22 June 2003.

[19] J. Ryu, "Resolution improvement in optical microscopy by use of multi-beam interferometric illumination," Ph.D. dissertation (Massachusetts Institute of Technology, Cambridge, Mass., 2003).

[20] M. Howells, J. Kirz, D. Sayre, and G. Schmahl, "Soft-x-ray microscopes," Physics Today **38**, 22–32 (August, 1985).

[21] J. Kirz, C. Jacobsen, and M. Howells, "Soft x-ray microscopies and their biological applications," Quarterly Reviews of Biophysics **28**, 33–130 (1995).

[22] D. Attwood, *Soft X-Rays and Extreme Ultraviolet Radiation: Principles and Applications* (Cambridge University Press, Cambridge, 1999).

[23] J. Susini, D. Joyeux, and F. Polack, eds., "7th International Conference on X-Ray Microscopy," Journal de Physique IV (Proceedings) **104** (2003).

[24] P. Kirkpatrick and A. V. Baez, "Formation of Optical Images by X-rays," Journal of the Optical Society of America **38**, 766–774 (1948).

[25] J. H. Underwood and D. T. Attwood, "The renaissance of x-ray optics," Physics Today **37**, 37–52 (April, 1984).

[26] W. Chao, E. H. Anderson, G. Denbeuax, B. Harteneck, J. A. Liddle, D. Olynick, A. L. Perason, F. Salmassi, C. Song, and D. Attwood, "20-nm-resolution soft x-ray microscopy demonstrated by use of multilayer test structures," Opt. Lett. **28**, 2019–2021 (2003).

[27] W. Chao, E. H. Anderson, G. Denbeuax, B. Harteneck, A. L. Perason, D. Olynick, F. Salmassi, C. Song, and D. Attwood, "Demonstration of 20 nm half-pitch

spatial resolution with soft x-ray microscopy," J. Vac. Sci. Technol. B **21**, 3108–3111 (2003).

[28] A. N. Kurokhtin, A. V. Popov, "Simulation of high-resolution x-ray zone plates," J. Opt. Soc. Am. A **19**, 315–324 (2002).

[29] J. Miao, T. Ishikawa, B. Johnson, E. H. Anderson, B. Lai, and K. O. Hodgson, "High resolution 3D x-ray diffraction microscopy," Phys. Rev. Lett. **89**, 088303 (2002).

[30] L. Kipp, M. Skibowski, R. L. Johnson, R. Berndt, R. Adelung, S. Harm, and R. Seemann, "Sharper images by focusing soft X-rays with photon sieves," Nature **414**, 184–188 (2001).

[31] S. Fields, "Proteomics in Genomeland," Science **291**, 1221–1224 (2001).

[32] H. Frauenfelder, "Proteins: Paradigms of Complexity," PNAS **99**, 2479–2490 (2002).

[33] B. Bailey, V. Krishnamurthi, D. L. Farkas, D. L. Taylor, and F. Lanni, "Three-dimensional imaging of biological specimens with standing wave fluorescence microscopy," Proc. SPIE **2184**, 208–213 (1994).

[34] V. Krishnamurthi, B. Bailey, and F. Lanni, "Image processing in 3D standing-wave fluorescence microscopy," Proc. SPIE **2655**, 18–25 (1996).

[35] R. Freimann, S. Pentz, and H. Hörler, "Development of a standing-wave fluorescence microscope with high nodal flatness," Journal of Microscopy **187**, 193–200 (1997).

[36] C. J. R. Sheppard and A. Choudhury, "Image formation in the scanning microscope," Optica Acta **24**, 1051–1073 (1977).

[37] J. W. Goodman, *Introduction to Fourier Optics* (McGraw Hill, New York, 1996).

[38] M. Nagorni and S. W. Hell, "Coherent use of opposing lenses for axial resolution increase in fluorescence microscopy. I. Comparative study of concepts," J. Opt. Soc. Am. A **18**, 36–48 (2001).

[39] A. R. Thompson, *Interferometry and Synthesis in Radio Astronomy* (Wiley, New York, 2001).

[40] E. Keto, "The shapes of cross-correlation interferometers," Astrophys. J **475**, 843–852 (1997).

[41] R. H. Jordan and D. G. Hall, "Free-space azimuthal paraxial wave equation: the azimuthal Bessel-Gauss beam solution," Opt. Lett. **19**, 427–429 (1994).

[42] Z. Bouchal and Marek Olivík, "Non-diffractive vector Bessel beams," Journal of Modern Optics **42**, 1555–1566 (1995).

[43] M. Bertero, P. Boccacci, G. J. Brakenhoff, F. Malfanti, and H. T. M. van der Voort, "Three-dimensional image restoration and super-resolution in fluorescence confocal microscopy," Journal of Microscopy **157**, 3–20 (1990).

[44] S. W. Hell and M. Nagorni, "4Pi confocal microscopy with alternate interference," Opt. Lett. **23**, 1567–1569 (1998).

[45] S. W. Hell, C. M. Blanca, and Jörg Bewersdorf, "Phase determination in interference-based superresolving microscopes through critical frequency analysis," Opt. Lett. **27**, 888–890 (2002).

[46] M. R. S. Bulletin **29** (Special Issue), 152–181 (2004).

[47] W. Yun, B. Lai, Z. Cai, J. Maser, D. Legnini, E. Gluskin, Z. Chen, A. A. Krasnoperova, Y. Vladimirsky, F. Cerrina, E. Di Fabriozio, and M. Gentili, "Nanometer focusing of hard x rays by phase zone plates," Rev. Sci. Instrum. **70**, 2238–2241 (1999).

[48] J. J. Rocca, "Table-top soft x-ray lasers," Rev. Sci. Instrum. **70**, 3799–3827 (1999).

[49] Y. Liu, M. Seminario, F. G. Tomasel, C. Chang, J. J. Rocca, and D. T. Attwood, "Achievement of essentially full spatial coherence in a high-average-power soft-x-ray laser," Phys. Rev. A **63**, 033802 (2001).

[50] P. G. O'Shea and H. P. Freund, "Free-Electron Lasers: Status and Applications" Science **292**, 1853–1858 (2001).

[51] R. A. Bartels, A. Paul, H. Green, H. C. Kapteyn, M. M. Murnane, S. Backup, I. P. Christov, Y. Liu, D. Attwood, and C. Jacobsen, "Generation of Spatially Coherent Light at Extreme Ultraviolet Wavelengths," Science **297**, 376–378 (2002).

[52] H. C. Kapteyn and T. Ditmire, "Ultraviolet upset," Nature **420**, 467–468 (2002).

[53] L. Mandel and E. Wolf, *Optical coherence and quantum optics* (Cambridge University Press, Cambridge, 1996).

[54] K. E. Oughstun, ed., *Selected papers on scalar wave diffraction* (SPIE Optical Engineering Press, Bellingham, Wash., 1992).

[55] J. Durnin, "Exact solutions for nondiffracting beams. I. The scalar theory," J. Opt. Soc. Am. A **4**, 651–2654 (1987).

[56] P. P. Naulleau, K. A. Goldberg, P. Batson, J. Bokor, P. Denham, and S. Rekawa, "Fourier-synthesis custom-coherence illuminator for extreme ultraviolet microfield lithography," Appl. Opt. **42**, 820–826 (2003).

[57] S. Quabis, R. Dorn, M. Eberler, O. Glöckl, and G. Leuchs, "Focusing light to a tighter spot," Opt. Commun. **179**, 1–7 (2000).

[58] N. Bokor and N. Davidson, "Toward a spherical spot distribution with 4π focusing of radially polarized light," Opt. Lett. **29**, 1968–1970 (2004).

[59] R. Dorn, S. Quabis, and G. Leuchs, "Shaper focusing for a radially polarized light beam," Phys. Rev. Lett. **91**, 233901 (2003).

[60] C. Debus, M. A. Lieb, A. Drechsler, and A. J. Meixner, "Probing highly confined optical fields in the focal region of a high NA parabolic mirror with subwavelength spatial resolution," Journal of Microscopy **210**, 203–208 (2003).

[61] N. Davidson and N. Bokor, "High-numerical-aperture focusing of radially polarized doughnut beams with a parabolic mirror and a flat diffractive lens," Opt. Lett. **29**, 1318–1320 (1994).

[62] T. Grosjean, D. Courjon, and D. Van Labeke, "Bessel beams as virtual tips for near-field optics," Journal of Microscopy **210**, 319–323 (2002).

[63] R. Oron, S. Blit, N. Davidson, A. A. Friesem, Z. Bomzom, and E. Hasman, "The formation of laser beams with pure azimuthal or radial polarization," Appl. Phys. Lett. **77**, 3322–3324 (2000).

[64] S. Quabis, R. Dorn, M. Eberler, O. Glöckl, and G. Leuchs, "The focus of light — theoretical calculation and experimental tomographic reconstruction," Appl. Phys. B **72**, 109–113 (2001).

[65] S. W. Hell and E. H. K. Stelzer, "Properties of a 4Pi confocal fluorescence microscope," J. Opt. Soc. Am. A **9**, 2159–2166 (1992).

[66] W. V. Houston, "A compound interferometer for fine structure work," Phys. Rev. **29**, 478–484 (1927).

[67] A. J. den Dekker and A. van den Bos, "Resolution: a survey," J. Opt. Soc. Am. A **14**, 547–557 (1997).

[68] D. Attwood, G. Sommargren, R. Beguiristain, K. Nguyen, J. Bokor, N. Ceglio, K. Jackson, M. Koike, and J. Underwood, "Undulator radiation for at-wavelength interferometry of optics for extreme-ultraviolet lithography," Appl. Opt. **32**, 7022–7031 (1993).

[69] H. H. Solak, D. He, W. Li, and F. Cerrina, "Nanolithography using extreme ultraviolet lithography interferometry: 19 nm lines and spaces," J. Vac. Sci. Technol. B **17**, 3052–3057 (1999).

[70] C. Chang, P. Naulleau, E. Anderson, and D. Attwood, "Spatial coherence properties of undulator radiation based on Thompson-Wolf two-pinhole measurement," Nucl. Instr. and Meth. A **467–468**, 913–916 (2001).

[71] D. Paterson, B. E. Allman, P. J. McMahon, J. Lin, N. Moldovan, K. A. Nugent, I. McNulty, C. T. Chantler, C. C. Retsch, T. H. K. Irving, and D. C. Mancini, "Spatial coherence measurement of X-ray undulator radiation," Opt. Commun. **195**, 79–84 (2001).

[72] J. J. A. Lin, D. Paterson, A. G. Peele, P. J. McMahon, C. T. Chantler, K. A. Nugent, B. Lai, N. Moldovan, Z. Cai, D. C. Macini, and I. McNulty, "Measurement of the Spatial Coherence Function of Undulator Radiation using a Phase Mask," Phys. Rev. Lett. **90**, 074801 (2004).

[73] J. J. Rocca, J. Dunn, and S. Suckewer, eds., *X-Ray Lasers 2002: 8th International Conference on X-ray Lasers* (American Institute of Physics, Mellville, New York, 2002).

[74] E. E. Fill and S. Suckewer, eds., "Soft X-ray Lasers and Applications V," Proc. SPIE **5197** (2003).

[75] Z. Chang, A. Rundquist, H. Wang, M. M. Murnane, and H. C. Kapteyn, "Generation of Coherent Soft X Rays at 2.7 nm Using High Harmonics," Phys. Rev. Lett. **79**, 2969–2970 (1997).

[76] A. Rundquist, C. G. Durfee III, Z. Chang, C. Herne, S. Backus, M. M. Murnane, and H. C. Kapteyn, "Phase-Matched Generation of Coherent Soft X-rays," Science **280**, 1412–1415 (1998).

[77] E. A. Gibson, A. Paul, N. Wagner, R. Tobey, D. Gaudiosi, S. Backus, I. P. Christov, A. Aquila, E. M. Gullikson, D. T. Attwood, M. M. Murnane, and H. C. Kapteyn, "Coherent Soft X-ray Generation in the Water Window with Quasi-Phase Matching," Science **302**, 95–98 (2003).

[78] D. L. Matthews, P. L. Hagelstein, M. D. Rosen, M. J. Eckart, N. M. Ceglio, A. U. Hazi, H. Medecki, B. J. MacGowan, J. E. Trebes, B. L. Whitten, E. M. Campbell, C. W. Hatcher, A. M. Hawryluk, R. L. Kauffman, L. D. Pleasance, G. Rambach, J. H. Scofield, G. Stone, and T. A. Weaver, "Demonstration of a Soft X-Ray Amplifier," Phys. Rev. Lett. **54**, 110–114 (1985).

[79] C. D. Macchietto, B. R. Benware, and J. J. Rocca, "Generation of millijoule-level soft x-ray laser pulses at a 4-Hz repetition rate in a highly saturated tabletop capillary discharge amplifier, Opt. Lett. **24**, 1115-1117 (1999).

[80] Nucl. Instr. and Meth. A **500** (Special Section), 1–40 (2003).

[81] F. Schäfers, M. Mertin, D. Abramsohn, A. Gaupp, H.-Ch. Mertins, and N. N. Salashchenko, "Cr/Sc nanolayers for the water window: improved performance," Nucl. Instr. and Meth. A **467–468**, 349–353 (2001).

[82] F. Eriksson, G. A. Johansson, H. M. Hertz, E. M. Gullikson, U. Kreissig, and J. Birch, "14.5% near-normal incidence reflectance of Cr/Sc x-ray multilayer mirrors for the water window," Opt. Lett. **28**, 2494–2496 (2003).

[83] E. Spiller, *Soft X-Ray Optics* (SPIE Optical Engineering Press, Bellingham, Wash., 1994).

[84] S. S. Hong, "Surface Acoustic Wave Optical Modulation," M.Eng. thesis, Massachusetts Institute of Technology, Cambridge, Mass., 2001.

[85] S. S. Hong, M. S. Mermelstein, and D. M. Freeman, "Reflective acousto-optic modulation with surface acoustic waves," Applied Optics **43**, 2920–2924 (2004).

[86] R. Henderson, "The potential and limitations of neutrons, electrons and x-rays for atomic-resolution microscopy of unstained biological molecules," Quarterly Reviews of Biophysics **28**, 171–193 (1995).

[87] G. Schneider, "Cryo X-ray microscopy with high spatial resolution in amplitude and phase contrast," Ultramicroscopy **75**, 85–104 (1998).

[88] W. Meyer-Ilse, D. Hamamoto, S. A. Liliévre, G. Denbeaux, L. Johnson, A. L. Pearson, D. Yager, M. A. Legros, and C. A. Larabell, "High resolution protein localization using soft X-ray microscopy," Journal of Microscopy **201**, 395–403 (2000).

[89] J. Drenth, *Principles of Protein X-Ray Crystallography* (Springer, New York, 1999).

[90] C. G. Schroer, P. Cloetens, M. Rivers, A. Snigirev, A. Takeuchi, and W. Yun, "High-Resolution 3D Imaging Microscopy Using Hard X-Rays," M. R. S. Bulletin **29**, 157–165 (2004).

[91] J. C. Dainty, ed., *Laser Speckle and Related Phenomena, 2nd ed.* (Springer-Verlag, Berlin, 1984).

[92] H. H. Barrett and K. J. Myers, *Foundations of Image Science* (Wiley, New Jersey, 2004).

[93] A. V. Oppenheim and R. W. Schafer, *Discrete-Time Signal Processing* (Prentice Hall, New Jersey, 1989).